A novel animal-borne miniature echosounder to observe the distribution and migration patterns of intermediate trophic levels in the Southern Ocean

Martin Tournier, Pauline Goulet, Nadège Fonvieille, David Nerini, Mark Johnson, Christophe Guinet

A novel animal-borne miniature echosounder to observe the distribution and migration patterns of intermediate trophic levels in the Southern Ocean

Martin Tournier[1], Pauline Goulet[2], Nadège Fonvieille[1,3], David Nerini[3], Mark Johnson[4], Christophe Guinet[1]

[1]Centre d'Etudes Biologiques de Chizé, CNRS-La Rochelle Université, UMR 7372, 79360 Villiers-en-Bois, France

[2]Sea Mammal Research Unit, University of St Andrews, St Andrews, Fife KY16 8LB, UK

[3]Aix-Marseille Université, CNRS/INSU, Université de Toulon, IRD, Mediterranean Institute of Oceanography UM 110, 13288 Marseille cedex 09, France

[4]Aarhus Institute of Advanced Studies, Aarhus University, Høegh-Guldbergs Gade 6B, 8000 Aarhus C, Denmark

Highlights:

- A novel sonar tag provides an acoustic scan of the elephant seal environment
- The sonar tag is able to detect common features such as the diel vertical migration of small organisms
- Contrasting oceanographic conditions affect the vertical distribution and abundance of mid-trophic level organisms
- Areas of high particle abundances were observed over 500 m, potentially corresponding to marine snow events

Abbreviations:

DSL: Deep-Scattering Layer, DVM: Diel Vertical Migration, FPCA: Functional Principal Component Analysis, KER: Kerguelen Islands, PV: Peninsula Valdes, MTL: Mid-Trophic Level, NSAF: Northern Sub-Antarctic Front, PCAs: Prey Capture Attempts, SAF: Sub-Antarctic Front, SO: Southern Ocean

Abstract

Despite expanding *in-situ* observations of marine ecosystems by new-generation sensors, information about intermediate trophic levels remains sparse. Indeed, mid-trophic levels, while encompassing a broad range of zooplankton and micronekton organisms that represent

a key component of marine ecosystems and sustain large and diverse communities of marine predators, are challenging to sample and identify. In this study, we examined whether an animal-borne miniature active echosounder can provide information on the distribution and movements of mid-trophic level organisms. If so, such a sonar tag, harnessing the persistent diving behaviour of far-ranging marine mammals, could greatly increase the density of data on this under-studied biome. High-frequency (1.5 MHz) sonar tags were deployed simultaneously with oceanographic tags on two southern elephant seals (*Mirounga leonina*), at the Kerguelen Islands and Valdés Peninsula (Argentina), and recorded acoustic backscatter while the seals foraged respectively in the Indian and the Atlantic sectors of the Southern Ocean. The backscatter varied widely over time and space, and the seals attempted to capture only a small fraction of the insonified targets. Diel vertical migration patterns were clearly identifiable in the data, reinforcing our confidence in the ability of the sonar tags to detect living mid-trophic organisms along with possibly sinking biological detritus. Moreover, CTD tags attached to the same animals indicated how the abundance, size distribution, and diel migration behaviour of acoustic targets varied with water bodies. These preliminary results demonstrate the potential for animal-borne sonars to provide detailed *in-situ* information. Further validation effort will make it a valuable tool to refine the estimation of carbon export fluxes as well as for assessing the variation of mid-trophic level biomass according to oceanographic domains and seasons.

Keywords: sonar tag, diel vertical migration, micronekton, marine acoustics, biologging, functional data analysis.

Introduction

Marine ecosystems are manifesting multi-level responses to oceanographic changes related to global warming, from a suspected shift in phytoplankton communities (Montes-Hugo *et al.* 2009, Barton *et al.* 2016) to top-predator population-size variations (Bost *et al.* 2015, Sydeman *et al.* 2015). However, assessment of the biological consequences of a changing ocean is hampered by a scarcity of information on the intermediate or mid-trophic levels (MTLs) (Hidalgo and Browman 2019). The crucial MTLs linking phytoplankton to upper

59 marine predators are composed of zooplankton and micronekton (e.g. mesopelagic fishes and
60 squids, euphausiids, siphonophores) (Handegard et al. 2009, Escobar-Flores et al. 2018)
61 presenting a wide range of body structures (e.g. crustaceans with a chitinous exoskeleton,
62 bony or gelatinous organisms), sizes (from a few millimetres for euphausiid larvae to a meter
63 for some siphonophores) and behaviours (e.g. planktonic or nektonic) (Sutton 2013, St. John
64 et al. 2016, Kloser et al. 2016). The mesopelagic biome, comprising a third of the global-
65 ocean volume, is one of the largest but least-known marine habitats (Reygondeau *et al.* 2018),
66 and considerable uncertainties remain regarding the total biomass of mesopelagic fishes.
67 Estimates of this biomass range from 2 to 20 gigatons (Irigoien *et al.* 2014, Kloser *et al.* 2016,
68 Proud *et al.* 2019), the latter being some 100 times the annual catch of all existing fisheries (
69 Anderson *et al.* 2019, Hidalgo and Browman 2019). The resulting scantiness of information
70 on the structure and turnover of mesopelagic food webs hinders accurate predictions about the
71 consequences of environmental changes or industrial fishing on this biome, and on the
72 numerous higher-level predators that it supports.
73

74 Information about the distribution and composition of MTLs is also critical for improved
75 estimates of carbon export fluxes. The Southern Ocean (SO) in particular plays a crucial role
76 in carbon sequestration, accounting for approximately 40% of global anthropogenic CO_2
77 uptake (DeVries 2014). The biological carbon pump operating in the SO remains only
78 partially explained due to the difficulty in monitoring its biotic environment, although recent
79 programmes such as KEOPS or CROZEX have proposed, in some parts of the SO, a
80 quantification of biological processes leading to carbon export (Blain *et al.* 2007, Pollard *et*
81 *al.* 2009, Salter *et al.* 2012, Le Moigne *et al.* 2016). The biological carbon pump begins with
82 primary production performed by phytoplankton, which represents the main source of organic
83 carbon exported to mesopelagic layers (Buesseler *et al.* 2007). Gravitational sinking of

84 phytoplankton as individual cells and aggregates is responsible for a significant portion of
85 carbon export in the SO (Leblanc *et al.* this issue, Laurenceau-Cornec *et al.* 2015a). However,
86 alternative biological mechanisms transporting the carbon trapped by phytoplankton to deep
87 waters are still poorly understood as they are likely to rely mainly on the behaviour of MTLs.

88 Of particular note with regard to MTL behaviour is the phenomenon of diel vertical migration
89 (DVM), which is performed by a large majority of MTL organisms, from small zooplanktonic
90 organisms to mesopelagic fish (Hays 2003, Sims *et al.* 2006, Watanabe *et al.* 2006), and is
91 found across all oceans (Behrenfeld *et al.* 2019). Representing the largest daily migration
92 observed in the biosphere (Brierley 2014), and presenting differences in migration patterns
93 depending on both the species and its life stage (Atkinson *et al.* 1992), DVM participates in a
94 massive carbon transfer across the mixed layers of the ocean (Buesseler and Boyd 2009,
95 Cavan *et al.* 2015, Aumont *et al.* 2018, Hernández-León *et al.* 2020). This vertical migration
96 pump results from MTL zooplankton and micronekton rising to the euphotic zone near the
97 surface where they generally feed at night. Carbon acquired at the surface is then actively
98 transported during the day to deeper waters where MTLs release rapidly-sinking faecal pellets
99 that form large aggregates (Belcher *et al.* 2017). This biological detritus gravitational flux, in
100 addition to active transport by MTL organisms, increases the transfer and transformation of
101 carbon (Cavan *et al.* 2015, Belcher *et al.* 2017, Cavan *et al.* 2019b), and contributes directly
102 to deep carbon sequestration. Preliminary estimates suggest that MTLs may be responsible for
103 about a quarter of carbon transport to deeper waters, though large uncertainties persist and
104 regional variability exists (Boyd *et al.* 2019). Achieving better quantification of the role
105 played by MTLs in the biological carbon pump is therefore still one of the current challenges
106 in oceanography.

107 Although advances in marine acoustics, especially in multi-frequency and multi-beam
108 echosounders, have resulted in a coarse classification of micronektonic organisms (Escobar-

Flores *et al.* 2019), the understanding of MTL taxonomic composition, biomass, and behaviour remains limited due to the difficulty of sampling. This is especially true for the SO where logistics and weather constrain ship-based operations. Consequently, acoustic and net-tow surveys of the mesopelagic layer, such as krill stock monitoring surveys (Fielding *et al.* 2014, Tarling *et al.* 2018, Manno *et al.* 2020), remain sparse for most SO sectors. In addition, although such surveys are highly valuable, they inevitably suffer from limited spatial and temporal coverage (Kloser *et al.* 2009). Each method also has its own sources of bias. Acoustic surveys are sensitive to regional differences in the relative abundance of mesopelagic species or in their body structure (Dornan *et al.* 2019). Net-tow sampling, which is often used to validate hydroacoustic surveys, suffers from an underestimation of energetic mesopelagic fishes that are able to escape the trawl (Kaartvedt *et al.* 2012, Proud *et al.* 2019), and rarely has sufficient spatial resolution to reveal mesoscale structuring (Davison *et al.* 2015). Although continuous ship-based acoustic surveys can sample over these larger spatial scales, they generally lack simultaneous sampling of fine-scale *in-situ* oceanographic profiles to investigate the coupling between physical and biological processes (Proud *et al.* 2019).

Helping to fill in the gaps left by ship-based surveys are autonomous ocean profilers (e.g. ARGO profilers and gliders), whose development has enabled extensive sampling of the physical properties of the water column. Recently some profilers were equipped to make continuous recordings of acoustic backscatter (Haëntjens *et al.* 2020). However, the relatively slow vertical movement of autonomous underwater robotic samplers may prevent reliable sampling of more rapid biological processes, such as the daily vertical migration of actively swimming larger-size micronekton species.

A creative approach to achieve dense sampling of physical oceanographic parameters in otherwise difficult-to-observe oceanographic regions has been to fit marine animals with

multi-sensor biologging tags so that they become ocean samplers (Fedak 2004, Hindell *et al.* 2016, Harcourt *et al.* 2019). Although this method does not provide systematic surveys, it offers the important advantage of providing simultaneous information about marine predator foraging ecology along with oceanographic conditions such as temperature, salinity or light level (Biuw *et al.* 2007, Guinet *et al.* 2014).

Biologging tags with sensors for temperature, salinity, chlorophyll-*a* concentration, and dissolved oxygen have yielded fine-scale descriptions of oceanic processes in remote areas (Roquet *et al.* 2013, Bayle *et al.* 2015, Bailleul *et al.* 2015). Southern elephant seals (*Mirounga leonina*, SES hereafter) are particularly useful for such sampling as they perform long-range foraging trips with continuous diving to mesopelagic depths, routinely reaching 1000 m and in rare cases exceeding 2000 m (Roquet *et al.* 2009, Hindell *et al.* 2016). In recent years, animal-borne sensors have been developed to quantify the marine organisms encountered by deep-diving mammals. High-resolution accelerometers have been used to detect prey capture attempts by SES (Guinet *et al.* 2014, Jouma'a *et al.* 2016), providing critical insight into interactions between these top predators and the MTLs. Importantly, this approach has opened the possibility of indirectly mapping the distribution of mesopelagic prey targeted by SES, in particular myctophid fish (Cherel *et al.* 2008, Vacquié-Garcia *et al.* 2015). While more detailed information on MTL prey encountered by northern elephant seals has been collected by camera tags (Naito *et al.* 2013), the high energy consumption of these devices has limited the amount of data that can be collected (Watanabe and Takahashi 2013). More recently, measurements of bioluminescence from some SES prey (Vacquié-Garcia *et al.* 2017, Goulet *et al.* 2020) have provided a means to distinguish classes of prey and their distribution. However, although these biologging approaches provide insight into the specific MTL prey targeted by SES (Yoshino *et al.* 2020), they offer little general information about the distribution of other MTL organisms. New perspectives are now offered by the miniature

159 animal-attached echosounder used in our study. This sonar tag was deployed on female SES
160 to study mesopelagic predator-prey interactions (Goulet *et al.* 2019). It can detect echoes from
161 small organisms (ranging from a few millimetres to tens of centimetres) over a short distance
162 (up to 6 m) in front of the seal, resulting in detailed profiles of sonar backscatter as the animal
163 dives. Here, we use data recorded by the tag on two SES females to assess the biological
164 conditions as they forage in contrasting oceanographic regimes off Patagonia (Argentina) and
165 the Kerguelen Islands. The goal of this study is to assess whether hydroacoustic data collected
166 from deep-diving SES can contribute to understanding pelagic ecosystems in the SO by: 1)
167 measuring the variation of MTL abundance and acoustic size within the water column; 2)
168 documenting the diel vertical migration of MTLs; and 3) mapping spatial variations in MTL
169 abundance and behaviour, and their relationships to local oceanographic conditions. While the
170 aim of the present study is not to quantify carbon fluxes, which is beyond the scope of this
171 paper and not possible at present, it can provide qualitative information on some processes
172 that are involved in controlling these fluxes.

173

174 **Material and methods**

175 1. Study sites and logger deployments

176 In October 2018, adult female SES breeding at Peninsula Valdes (Argentina, 42°57'S,
177 63°59W, abbreviated to PV) and on the Kerguelen Islands (49°21'S, 70°13'E, abbreviated to
178 KER) were fitted with biologgers using a standard procedure (McMahon *et al.* 2008). The
179 animals were captured and anaesthetised with an injection of Zoletil100 (1:1 mix of tiletamine
180 and zolazepam). In each study location, three biologging devices were glued to the animal's
181 fur using quick-setting epoxy (Araldite AW 1201): a head-mounted sonar tag (Goulet *et al.*
182 2019), a back-mounted Satellite Relayed Data Logger (CTD-SRDL, Sea Mammal Research

Unit, St Andrews, UK), and an ARGOS transmitting tag (SPOT, Wildlife Computers, USA). The CTD-SRDL recorded conductivity, temperature, and pressure at 1 Hz while also sending summary data via ARGOS messages. The SPOT tag was included to facilitate recovery of the tags when animals returned to land, in case the CTD-SDRL had stopped transmitting. At–sea movements were monitored using the ARGOS satellite-tracking system, and the loggers were recovered as soon as the seals hauled out for moulting. The three loggers had a total mass of under 800 g, representing less than 0.5% of the animal weight, and should therefore have minimal impact on the survival or foraging success of equipped animals (McMahon *et al.* 2008).

The sonar tag recorded high-resolution sonar, location, and movement data. GPS positions were obtained at each surfacing. Pressure and triaxial magnetometer data were recorded at a sampling rate of 50 Hz while triaxial acceleration was recorded at 200 Hz. The active sonar had a centre frequency of 1.5 MHz and emitted 10 µs pings at a rate of either 12.5 (PV) or 25 (KER) pings per second, with a source level of approximatively 187 dB re 1 µPa at 1 m (Goulet *et al.* 2019). Sound was transmitted and received via a transducer with a -3 dB beamwidth of approximately 3.4 degrees. The complex returning signal was demodulated and the resulting baseband signal was sampled at 192 kHz for intervals of 8 ms following each ping, giving a spatial resolution of about 3.9 mm and a maximum range of 6 m (see Goulet *et al.* 2019 for device specifications). The sonar transducer on the tag has a rigid backing which does not compress with depth. Therefore, we assume that the performance of the transducer remains reasonably constant over the depth range explored by SES. More in-depth validation approaches are still in progress and will be the subject of future papers

In order to extend the recording duration, the sonar was switched on and off on a regular basis with a cycle of 5.5 h on and 5.5 h off for Kerguelen and 24 h on and 24 h off in Argentina. Both protocols provided a homogenous sampling of all periods of the day throughout the

recording duration. The sonar was activated at depths deeper than 50 m for Kerguelen and 15 m for Argentina. The CTD and sonar tags were synchronised by matching the depth data sampled by their respective pressure sensors following Le Bras *et al.* (2016).

2. Sonar data processing and analysis

The echo level was calculated by first removing the mean values of the in-phase and quadrature received signals, and then computed as the root-mean square of these two signals. Echogram images were constructed from the log of the echo level, with each pixel representing a sonar sample (i.e. 1/192000 s or 3.9 mm of round-trip travel). Similar to echograms obtained from traditional fishery echosounders, the vertical dimension of the echogram represents the range to targets while the horizontal dimension represents successive pings (Figure 1). Hereafter, any insonified object giving an echo will be referred to as a scatterer, regardless of its nature or size. From the echograms, the two following metrics were derived:

Scatterer count

The scatterer count is the number of pixels for which the echo level exceeds a threshold chosen to differentiate actual scatterers from background noise. For each sonar-on phase of the sonar data, the background noise level was calculated from the signal contained in the last meter of the sonar range. A visual inspection of the sonar data indicated that targets were rarely evident at this range due to high spreading and absorption losses. The echo level of all pixels in the ~4.6-5.6 m range were therefore fit to a Rayleigh distribution to characterise the noise floor, and the detection threshold was set to the 99.9 percentile of this distribution (Figure 2, Supplementary Information). The scatterer number (SN) was then calculated as the total number of pixels above the detection threshold for each sonar ping, averaged over a 2-second window, resulting in a proxy for

232 absolute particle abundance. Scatterer abundance was then calculated as the standardised
233 SN divided by the nominal sampled volume, resulting in an approximate scatterer
234 abundance value, i.e. number per m^3. The sample volume was taken as the truncated cone
235 of the sonar beam in the 1-1.5 m range assuming a 3.4° beamwidth.

236 *Maximum apparent target size*

237 Acoustic studies often use the echo level as a proxy of the target size. In this study, it is
238 not possible to ascertain the position of small echoic targets in relation to the beam axis,
239 meaning that the echo level is dependent on the location, with the echo strength of a given
240 target decreasing as its position departs from the centre of the beam, and varying with the
241 orientation of the targets as well as their size and composition. However, the high spatial
242 resolution of the sonar data allowed measurement of the echo duration, which is related to
243 the target cross-section, shape and composition (Burwen *et al.* 2003). Apparent size was
244 therefore calculated for each detected scatterer using the duration Δt (s) for which the
245 echo intensity was above the detection threshold. This was converted to distance to give a
246 size estimate in metres: $\Delta t * ss/2 = size$, with ss = sound speed in seawater, taken as a
247 constant 1500 m/s throughout the record. For each 2-second period, the scatterer with the
248 largest apparent size was retained as the Maximum Apparent Size (MAS). Although the
249 smallest organic particle size detectable by the sonar tag is about 1 to 2 mm (L. Petiteau,
250 personal communication, Supplementary Information, Figure 4), the smallest apparent
251 size that can be calculated is 3.9 mm due to the limited sonar resolution. This spatial
252 resolution allows, in theory, the detection of most mesozooplanktonic organisms of high
253 ecological importance such as calanoids (e.g. *Rhincalanus gigas*), euphausiids (e.g.
254 *Euphausia vallentini*), hyperiids (e.g. *Themisto gaudichaudii*), gelatinous organisms (e.g.
255 *Rosacea plicata*). Considering that the sonar tag is able to detect targets as small as 1 mm
256 (see Supplementary Information), it is also probable that smaller copepods (e.g. *Calanus*

simillimus, *C. acutus*) contribute to the signal obtained. The apparent size is dependent on many factors including the distance, orientation and composition of the target, and its position relative to the beam axis, making this a noisy proxy for the real size. We therefore graded the MAS into two broad size classes based on the 'Sieburth-scale' plankton classes (Sieburth *et al.* 1978): the first class contained small scatterers with MAS up to 20 mm which we considered as mesoplankton-like objects. The second class contained objects with MAS ranging from 20 to 50 mm which were considered as small macroplankton. Objects with MAS larger than 50 mm were rare (representing 2.2% and 2.9% of the signal for PV and KER respectively) and were often associated with a jerk (i.e. rapidly changing acceleration signal) which most likely indicates a prey capture attempt (Ydesen *et al.* 2014). These large targets are therefore likely to be macronekton, including the mesopelagic fish and squids preyed upon by SES (Daneri and Carlini 2002). This latter size class was therefore removed from the analysis to focus on potentially zooplanktonic organisms.

The above sonar metrics were calculated over non-overlapping 2-second windows and extracted at distances ranging from 1 to 1.5 m ahead of the elephant seal's head. The lower distance limit was chosen to be beyond the sonar near-field and yet close enough to potentially detect echoes from the full-size range of MTL organisms. The 0.5 m analysis range was a trade-off between a narrower range, which may lead to too few detections for statistical evaluation, and a larger sampling range over which the probability of detection would vary substantially and hence complicate analysis.

Combining these acoustic metrics with the depth and GPS positioning collected by the tag resulted in a set of time-depth profiles similar to the oceanographic data profiles obtained with CTD loggers deployed on SES (Fedak 2004). The acoustic data were analysed with MATLAB R2019b, using custom functions.

3. Water body classification

A typology of the water bodies was established to investigate whether scatterer abundance on the one hand, and day versus night vertical distribution on the other hand, varied according to the oceanographic conditions encountered by the seal. Despite the good spatial and temporal resolution of SO fronts position estimation (Sallée *et al.* 2008), finer-scale structures, such as sub-mesoscale eddies or meanders, can have a strong impact on biological structure at a more local scale (Chapman *et al.* 2020), and by extension on the foraging behaviour of SES (Della Penna *et al.* 2015, Siegelman *et al.* 2019). Pauthenet *et al.* (2017) demonstrated that high-resolution oceanographic data sampled by CTD tags on SES can be used to objectively define the geographical extents of water bodies by analysing joint variation of temperature (T) and salinity (S). We therefore produced profiles of temperature and salinity for each dive, and fit B-splines to the sampled points. The structural variability between the splines was evaluated using the functional principal component analysis (FPCA) method developed by Ramsay and Silverman (2005), which is similar to a principal component analysis except that B-spline coefficients are used instead of raw data. Usage of FPCA enabled us to retain information about the shape of the temperature and salinity profiles (Nerini and Ghattas 2007, Pauthenet *et al.* 2017) while also allowing comparison between locations and individuals by smoothing out irregularities in data sampling.

Temperature and salinity profiles were generated on a constant vertical grid from 20 m to 200 m. This depth range was chosen to maximise temporal coverage especially at night when SES make shallower dives. As the objective of this analysis step was to describe near-surface mesoscale oceanic features that may influence MTL distribution, information loss on water structures below 200 m was not critical to our study. Dives shallower than 200 m were therefore removed. Oceanographic profiles were then decomposed on a B-spline basis with c coefficients estimated by polynomial regression (see Ramsay and Silverman 2005). The

FPCA method was applied to the set of coefficients resulting in a compact representation of each profile according to its degree of similarity to the first principal components (PCs) generated by the FPCA.

Clusters of similar curves were discriminated using k-means supervised classification. The classification of temperature and salinity curves was achieved in the space of the 5 first PCs. These PCs account for more than 90% of the total inertia and 98 % and 91.5% of the entire variability for KER and PV, respectively. Based on the Ward criterion, minimising the total within-cluster variance, we determined the number k of clusters for each SES track, with a maximum of five groups (Murtagh and Legendre 2014). Different clusters were considered as representing different water bodies and were then projected to their geographical positions along the track of the elephant seal, and did not necessarily correspond to the water bodies traditionally identified in these regions by other studies (Carter *et al.* 2008)

4. Analysis of vertical distribution

Each scatterer sampled by the sonar tag was assigned to a given water body as defined by the cluster analysis, according to the oceanographic conditions in which they were encountered. Although SES perform long-range foraging trips, they only travel a few tens of kilometres per day. This pace allows capturing large-scale phenomena such as mesozooplankton swarms (Fielding *et al.* 2014), and also the daily DVM, which is relatively consistent in the same water body (Behrenfeld *et al.* 2019). Migration behaviour, however, is suspected to be dependent on the organism type, which may lead to a time-varying vertical distribution of different-sized scatterers. We therefore determined the relative abundance in the water column of each scatterer size class (i.e. smaller than 20 mm and from 20 to 50 mm) according to the period of the day. As the prey of SES performed DVM as well, and were shallower at night, the sampling effort for the lower depths was unbalanced between day and night. The

day period was determined using the sun angle for the current position of the seal (Guinet *et al.* 2014). Then, for each water body, the mean abundance of each scatterer class for each 10-metre depth bin was calculated. The percentage difference between day and night means in each depth bin was computed to summarise the relative difference in migration behaviour for the two size classes.

The intensity of the DVM, for each water type, was determined by comparing the depth range of the migration (i.e. vertical amplitude), the total estimated abundance of scatterers present in the water column, and the mean acoustic size composition over the same depth range. For each profile, the depth with the highest abundance of scatterers was considered to represent the depth containing most of the organisms participating in the DVM. For each dive, the vertical distribution of the scatterers was determined by a simple peak-finding procedure. In most dives the vertical distribution of abundance was unimodal. In the case of a multimodal distribution, the largest mode was taken as the depth of maximum abundance. For each location, the range between the deepest and the shallowest abundance maximum was defined as the DVM range. Over these DVM ranges, the total abundance of scatterers was estimated by adding up interpolated values of the abundance for each depth meter. Finally, the mean size of the scatterers over the same depth ranges was compared between day and night in each water body. The numbers of samples for the different possible combinations of analysis categories (i.e. day period and water body) were unbalanced and heteroscedastic. Therefore, analyses assessing the effect of the period of the day and the water body were conducted using a multiway rank-based analysis (Rfit, Kloke and McKean 2012). Considering the large oceanographic differences between KER and PV regions, analyses were performed separately for each location, to compare DVM range, total abundance and size composition. Analyses were carried out with R software (R 3.5 R core team 2019).

Results

1. Sonar observations

The maximum depth and mean (± standard deviation) diving depths were respectively 936 m and 413 ± 136 m for KER individual with a mean diving depth of 321 ± 109 m at night and 499 ± 105 m during the day, and 1109 m and 392 ± 249 m for PV individual with a mean diving depth of 218 ± 108 m at night and 539 ± 272 m during the day. A total of 313.8 and 408.8 hours of sonar data for KER and PV, respectively, were analysed. The abundance of scatterers ranged from 7 to 11940 scatterers.m^{-3} in KER (mean = 490 ± 530 and from 13 to 13800 scatterers.m^{-3} in PV (mean = 795 ± 1465). The echo signal was dominated by small objects (< 20 mm), representing 52.4% of scatterers in KER and 93.9% in PV, whereas the 20-50 mm size class represented 44.7% and 5.6% of the objects detected in KER and PV respectively.

The signals recorded by the sonar tag showed wide variability with time and depth (Figures 2 and 3). Scatterer abundance was the highest in the upper 200 m of the water column in both regions, for both day and night.

A portion of the KER recording (Nov 11^{th}-15^{th}, Figure 2) showed an unusually high abundance of scatterers throughout the entire water column (from 70 m to 500 m) (Figures 1.b & 1.c). Over these 4 days, the mean size of the scatterers was 12 ± 4.5 mm.

A DVM pattern appeared to be the main driver of the vertical heterogeneity of the PV sonar signal data, in terms of scatterer abundance (Figures 3 and 5). This feature was not as clear for the KER dataset (Figures 2 and 4).

2. Classification of water bodies and scatterer size differences

A total of 2094 and 2819 dives for KER and PV, respectively, were used for the FPCA procedure (representing 96.9% and 85.5% of the available profiles; the remaining profiles did not reach 200 m).

The first two principal components (PC) accounted for 80.1% and 89% of the variability in the individual profiles for PV and KER, respectively. CTD profiles were distributed within three water clusters for PV, with 226, 1819, and 364 profiles recorded for water clusters 1, 2, and 3, respectively. The water bodies were distributed along both temperature and salinity gradients, with, for each location, colder and less salty waters for cluster 1 and warmer and saltier waters for cluster 3 (Figure 6).

3. Analyses of vertical distribution

When considering all scatterers regardless of size, the mean vertical extent of the abundance maximum ranged from 30 to 260 m in PV (Figure 7) while a narrower depth range from 70 m (i.e. the turn-on depth of the sonar) to 160 m was observed at KER (Figure 8).

For KER, there was a significant difference in the depth of peak abundance between day and night (p-value > 0.001), but no significant variation in depth between clusters (Figure 8). However, significant differences in scatterer abundance were found between water clusters (p-value < 0.005). The mean size of scatterers differed significantly across water clusters, but no diel differences in this parameter were observed. Larger scatterer sizes were encountered in water clusters 1 (14.7 ± 5 mm) and 2 (14.8 ± 3.7 mm) compared to water cluster 3 (11.8 ± 3.8 mm) (p-value < 0.001).

For PV, due to the 24-hour duty-cycle, no sonar profile was available for the night period of water cluster 1. For daylight hours, the depth of the main abundance peak differed significantly between the 3 water clusters (p-value < 0.001), with a deeper location in water clusters 2 and 3 compared to water cluster 1 (p-value < 0.001). Furthermore, the depth of the abundance maximum was significantly deeper during the day than the night for water clusters 2 and 3 (day: 113 ± 56.5 m, night: 42.3 ± 18.9 m, p-value < 0.001, for water cluster 2; day: 126 ± 49 m, night: 40.1 ± 13.1 m, p-value < 0.001 for water cluster 3; Figure 7b). The total number of scatterers, totalled over the depth range 30:260 m, was also significantly different between day and night for these water clusters (day: $194.10^3 \pm 48.10^3$, night $185.10^3 \pm 52.10^3$ for water cluster 2; day: $250.10^3 \pm 68.10^3$, night $125.10^3 \pm 46.10^3$ scatterers.m^{-3}, for water cluster 3, Figure 7c), but did not differ significantly between them. However, significant differences in scatterer size were found between the three clusters during the day (p-value > 0.001) when they could be compared (water cluster 1: 15.4 ± 6.6 mm, water cluster2: 10.7 ± 5.4 mm, water cluster 3: 11.5 ± 5.4 mm, Figure 7d).

The percentage difference between day and night for each scatterer size class in 10-metre depth bins showed a regular pattern of maximum abundance in upper layers at night, and in lower layers during the day (Figure 9). Depending on the water body, small (i.e. < 20 mm) and medium-sized (20-50 mm) scatterers exhibited some differences in their vertical distribution patterns (Figure 9).

Finally, clear differences were evident between KER and PV when looking at the complete depth range of 70 to 260 m that was sampled during the two surveys. Although the average scatterer abundance was similar in the two locations, PV data exhibited greater differences between the day and night vertical distributions of scatterers (p-value < 0.001, Figure 10a). However, the mean size of scatterers was greater for KER (25.1 ± 7.1 mm, max = 175 mm) compared to PV data (17.4 ± 6.2 mm, p-value < 0.05, max = 351 mm, Figure 10b).

Discussion

1. Horizontal and vertical heterogeneity in the acoustic backscatter

Two sonar tags were deployed in parallel on elephant seals from distinct oceanographic regions to assess their performance in capturing the sizes, vertical distribution and diel dynamics of MTL organisms. While a previous study showed that mesopelagic fish/squids were detected by the sonar tag during close prey encounters (Goulet *et al.* 2019), the present study quantifies the abundance of smaller acoustic targets, insonified by the tags as the seals dived through the water column. The primary aim of this study, presenting the first-ever application of the new biologger, is therefore to assess its potential for quantifying the vertical and horizontal distribution of the MTLs during the far-ranging foraging trips of SES.

It is important to note that using a free-ranging foraging animal as a sampling platform may ineluctably lead to some sampling bias. Foraging SES tend to target, and therefore oversample, highly dynamic areas such as fronts (Cotté *et al.* 2015, Della Penna *et al.* 2015, Rivière *et al.* 2019) characterised by complex hydrodynamic conditions, which are favourable for prey aggregation. In contrast, SES may tend to undersample areas of lower organism concentrations. However, this prey bias was reduced in this study by excluding portions of the sonar signal corresponding to prey catch attempts. As a result, only MTL organisms which were not targeted by the SES were investigated in the present study. Conversely, it should also be noted that some of the sampling biases associated with the use of non-biological platforms, such as gliders or Argo floats, are absent when using animal platforms. For example, Haëntjens *et al.* (2020) report a possible attraction of MTL organisms to the LEDs used on Argo floats, which is avoided by the sonar tag without LEDs. In addition, the slow

449 descent speed of a float is likely to cause a gathering of organisms in the echosounder beam,
450 whereas the vertical speed of the elephant seal of about 1.4 m/s prevents any flock formation.

451 A comparison between an underwater vision profiler and a sonar tag for measuring organism
452 abundance has revealed the sonar tag's ability to detect organisms as small as 1 mm in
453 diameter (unpublished data; Petiteau in prep., Supplementary Information). However, it is
454 important to underline that the method used in this study cannot distinguish between several
455 small, closely aggregated targets (i.e. separated by less than 3.9 mm, the spatial resolution of
456 the sonar), and a single target of the same apparent size. Nevertheless, as the deep-water
457 environments visited by foraging SES contain relatively few particles, the first scenario is
458 rarely encountered, and should contribute only slightly to overall abundance estimates. Given
459 the potential range of backscatter sources, the sonar tag data from SES in KER and PV likely
460 include backscatter from a combination of objects whose nature cannot be determined,
461 whether biological debris passively sinking to the ocean floor, or living organisms, some of
462 them undertaking diel vertical migrations.

463 The main limitations being stated, we found that scatterers were more abundant and produced
464 higher-intensity echoes in the upper part of the water column (i.e. above 250 m deep) in both
465 locations. Temporal variations of the backscatter distribution were consistent with a daily
466 cyclic movement in the water column corresponding to the daily migration of MTL
467 organisms. However, this diel signal was not evident continuously throughout the datasets,
468 and so is likely dependent on the nature of the scatterers present locally. Specifically, when
469 the backscatter is dominated by small-size non-migrating items, we suggest that this could be
470 indicative of biological detritus or else small-size non-vertically-migrating zooplankton, such
471 as *Calanus propinquus* (Conroy *et al.* 2020), highly abundant in the eastern sector of the
472 Kerguelen shelf (Carlotti *et al.* 2008).

We also found evidence that both the horizontal and vertical distributions of scatterers vary according to the oceanographic conditions encountered. Five distinct water bodies were identified along the seal tracks, corresponding closely with weekly estimates of SO fronts positions (Sallée *et al.* 2008). Only one of these water bodies, water body 3, corresponding to Sub-Antarctic Waters (SAW), was encountered by seals from both KER and PV. Each seal also encountered two other water types but these were distinct in each location.

For the PV seal, clear differences in the vertical distribution, abundance and size of scatterers were found between each oceanographic domain visited, evidencing a change in MTL community composition and/or abundance depending on the water body. The changes in water body along the track may indicate that the seal encountered sub-mesoscale oceanographic features. Such structures are frequently used by SES and are often linked with improved foraging conditions (Dragon *et al.* 2010, Della Penna *et al.* 2015, Siegelman *et al.* 2019). Currently, the datasets are too limited to investigate the commonalities and differences of scatterers among similar water bodies, or to investigate seasonal changes. We can nevertheless expect an increased number of deployments of this tag, and the large ranges covered by SES, to lead to studies comparing the different large-scale water bodies explored by SES.

2. Regional differences in sonar signal

In both study areas, the abundance of scatterers varied depending on the water body. For the PV seal, significantly higher scatterer abundance was found in water body 1, which was close to the continental shelf, compared to the two other water bodies it encountered. This might be related to the highly productive waters of the Patagonian continental shelf, which receive nutrient-enriched inputs from the Malvinas current and support a large spring bloom (Lutz *et al.* 2018) with likely enhanced secondary production (Cepeda *et al.* 2018). However, the prey

497 catch rate of the seal is low within this water body compared to elsewhere along its track,
498 suggesting that this high spring productivity may not lead to increased abundance of the prey
499 targeted by SES, or with a delay, due to the temporal decoupling of primary producers and
500 primary consumers (Latasa *et al.* 2014). Further offshore, within the Sub-Antarctic Front
501 (SAF) northward inclusion, primary production tends to be lower and supports communities
502 of small mesozooplankton with lower biomass (Thompson *et al.* 2013) — a tendency that
503 appears to be supported by the sonar tag data, revealing fewer and smaller scatterers with a
504 very clear DVM pattern.

505 Similarly, MTL abundance in KER differs according to water mass, with the lowest
506 abundance observed for water body 3 and the highest for water body 1. Water body 3
507 comprises profiles in the area around the North SAF and can be considered as a different
508 bioregion than the other water bodies influenced by the subtropical regime (Godet *et al.*
509 2020). The warmer waters of this region tend to be associated with lower chlorophyll-*a*
510 concentration and overall lower productivity than the high-productivity shelf and off-shelf
511 waters of the Kerguelen plateau (Godet *et al.* 2020). The high abundance of scatterers seen in
512 water body 1 may be associated with these enriched plateau waters, with eastward advection
513 by currents releasing soluble iron, and enhancing primary production (Robinson *et al.* 2016,
514 Schallenberg *et al.* 2018).

515 Overall, a higher abundance of larger-sized scatterers was encountered in KER compared to
516 PV waters while the DVM pattern is more obvious within the PV dataset. These findings
517 exemplify the differences between these two distinct marine provinces (Longhurst 2010, Fay
518 and McKinley 2014). Our results also highlight the wide variability in vertical distribution
519 patterns of the MTLs, a finding consistent with recent fine-resolution studies (Pinti and Visser
520 2018, Conroy *et al.* 2020) and global ocean studies (Behrenfeld *et al.* 2019). More extensive

521 deployments of the sonar tag may therefore help improve our understanding of the
522 environmental and biological factors that drive these differences.

523 3. Diel vertical migration

524 The current study also reveals fundamental differences in the vertical distribution and
525 behaviour of zooplanktonic and micronektonic organisms according to their sizes. A day-
526 scale cyclic vertical movement of a portion of the scatterers was evident in sections of the
527 sonar recordings (see Figures 4.b & 5.b) comprising an upward migration at dusk and a
528 downward one at dawn. The presence of this diel pattern in our data confirms the ability of
529 the sonar tag to detect mesopelagic organisms, such as macrozooplankton, or other small
530 MTL organisms involved in the DVM.

531 The extent of the vertical migration recorded by the sonar tag in both regions, reaching 160 m
532 deep in KER and 260 m deep in PV, does not match the migration range of mesopelagic fish
533 such as myctophids, and squid (Davison *et al.* 2015, Bianchi and Mislan 2016, Béhagle *et al.*
534 2016, Kloser *et al.* 2016), which is also revealed by the day and night mean diving depth of
535 the two seals. Therefore, the observed DVM likely represents the vertical movement of
536 zooplankton (i.e. the prey of SES prey) although inferences about the size of scatterers from
537 the sonar data require validation. However, the minimum spatial resolution of the sonar tag
538 (approx. 3.9 mm) means that smaller organisms will be lumped within the smallest size class
539 resolved by the sonar tag. Nonetheless, the mean acoustic size (2 to 3 cm) of the migrating
540 scatterers, and the depth range at which they are detected, suggest large zooplanktonic
541 organisms like euphausids. Indeed, the Kerguelen waters host high abundances of euphausids
542 (Cuzin-Roudy *et al.* 2014, Koubbi *et al.* 2016, Godet *et al.* 2020) such as *Thysanoessa*
543 *macrura* and *Euphausia vallentini*, both with an adult size close to 3 cm. The Argentinian
544 Patagonian waters also host high densities of *E. vallentini* (Cepeda et al. 2018). This krill

545 species makes a diel migration between 100 and 250 m depth (Cuzin-Roudy *et al.* 2014),
546 matching the vertical range of the migration detected by the sonar tag in this location.

547 4. A possible marine snow event recorded off Kerguelen

548 Between November 10th and 14th, the sonar tag deployed in KER recorded anomalously high
549 and constant scatterer abundances throughout the epipelagic layer to 500 m deep. This could
550 have been caused by large concentrations of salps (Wiebe *et al.* 2010), and validation of the
551 sonar tag is required to determine the typical echo signals generated by low-target strength
552 targets such as salps and jellyfish. However, the homogeneous distribution along the vertical
553 dimension could also indicate a mass sinking event of biological detritus, known as marine
554 snow (Alldredge and Silver 1988, Turner 2015). Marine snow events follow periods of high
555 productivity, when heavy phytoplankton cells and zooplankton faecal pellets sink downwards
556 rapidly (Laurenceau-Cornec *et al.* 2015b). Some studies suggest that these events, occurring
557 off the Kerguelen plateau twice a year during the seasonal blooms, represent, in the SO, one
558 of the main contributions to the biological pump that exports particulate organic carbon
559 (POC) to depth (Turner 2015, Rembauville *et al.* 2015). The spatial co-occurrence between
560 such events and satellite-assessed POC from remote sensing may help resolve this question in
561 the future (Tran *et al.* 2019).

562 5. Where is the Deep Scattering Layer?

563 A vast majority of the scatterers recorded by the sonar tags come from the epipelagic zone,
564 whereas beneath 300 m, in the mesopelagic layer, echoes were scarce. One of the most
565 notable acoustic features of the global ocean, the deep scattering layer (DSL), is therefore not
566 immediately evident in the sonar tag data. The DSL, mainly composed of mesopelagic fish
567 and squids (i.e. the main prey of SES), is found in the mesopelagic zone at a depth of around
568 400 to 500 m throughout the world oceans (Proud *et al.* 2018), and particularly in the SO

(Kloser *et al.* 2016, Béhagle *et al.* 2017). This depth is consistent with the mean diving depth of the SES, and the sonar tag's inability to detect the DSL as a clear pattern in the way that ship-based echosounders have been found to do, can possibly be explained by their different sampling resolutions. Ship echosounders are mainly designed to detect mesopelagic scatterers composed of organisms exceeding several centimetres while the high frequency sonar tag is well-suited to detect smaller-size organisms. Studies have established that the abundance of zooplankton and micronekton decreases linearly with size following a log/log function (Heneghan *et al.* 2016)). Therefore, due to its narrow beam, the water volume sampled by the sonar tag is limited and may prevent the relatively low densities of micronektonic fish and squids from being properly assessed. In comparison, ship-based echo-sounders have a larger beam and are operated from the surface, leading to a much greater insonified volume of water at greater depths. Such sonars are well suited to sample bulk micronekton but are not so well-suited to assess small-size and dispersed zooplankton. Therefore, these two approaches should be seen as complementary with one another. Nonetheless, the bottom phase of SES dives, and more specifically the depth of prey capture attempts (PCAs), provide a proxy for the DSL depth in the water column (Guinet *et al.* 2014, McMahon *et al.* 2019). Both the dive depth and the depth of PCAs, as inferred from acceleration transients recorded by biologging tags on SES, vary with a diel cycle, presumably tracking the daily vertical migration of components of the DSL (Figure 4.b and Figure 5.b). The sonar tags frequently recorded scatterers with a large apparent size simultaneously with PCAs. The focus of the study being smaller-size MTL organisms, and the time SES spend foraging being disproportionate, PCAs were excluded from this study. These larger scatterers however likely represent the DSL organisms targeted by SES and so provide some indication about the density and size distribution of the DSL that is the topic of a companion paper (Goulet *et al.*, in prep).

Conclusion

Although the sonar tag, aided by the persistent diving behaviour of SES, shows considerable promise for *in situ* studies of the biotic environment of the deep ocean, namely the distribution and movement of resident organisms, a recurring issue is the lack of certainty in inferring organism size and type from the echo returns. A key area for future work is therefore to assess how well the echo patterns associated with different sizes and categories of organisms can be distinguished with the current tag design. This information is critical for most trophic and carbon flux studies (Hernández-León *et al.* 2019). While careful tank-based validation studies can improve confidence in interpreting the sonar tag, ultimately *in situ* measurements will be most useful for the identification of unique deep-sea fauna that cannot be held in aquaria. One way to achieve *in situ* validation could be to combine the sonar tag with a camera tag in such a way that image capture is triggered by acoustic detections within a given detection range.

Acknowledgements

Marine mammal data were gathered by the international MEOP Consortium, including the French National Observatory Mammals as sampler of the Ocean Environment (SNO-MEMO). Fieldwork in Kerguelen was supported by the French Polar Institute (Institut Polaire Français Paul Emile Victor) as part of the CyclEleph programme (n. 1201, PI C.Gilbert). Fieldwork in Peninsula Valdes was supported by CNES-TOSCA (Centre National d'Études Spatial) as part of a French-Argentinian collaborative program (PI C. Guinet). This research was funded by the "Agence Innovation Défense" and the "Région Nouvelle-Aquitaine" to M.T.

The Kerguelen fieldwork team 2018-2019 as well as the Peninsular Valdes fieldwork team 2018-2019, who deployed and recovered the tags are gratefully acknowledged, with special thanks to J. Mestre, C. Vuillet, H. Allegue involved in the Kerguelen tagging, and to J. Campagna, C. Campagna, M.A. Hindell and C. Vera for the Argentinian deployments.

Declaration of interest:

The authors declare that they have no known competing financial interests or personal relationships that could have appeared to influence the work reported in this paper.

Alldredge, A. L., and M. W. Silver. 1988. Characteristics, dynamics and significance of marine snow. Progress in Oceanography 20:41–82.

Anderson, T. R., A. P. Martin, R. S. Lampitt, C. N. Trueman, S. A. Henson, and D. J. Mayor. 2019. Quantifying carbon fluxes from primary production to mesopelagic fish using a simple food web model. ICES Journal of Marine Science 76:690–701.

Atkinson, A., P. Ward, R. Williams, and S. A. Poulet. 1992. Feeding rates and diel vertical migration of copepods near South Georgia: comparison of shelf and oceanic sites. Marine Biology 114:49–56.

Aumont, O., O. Maury, S. Lefort, and L. Bopp. 2018. Evaluating the Potential Impacts of the Diurnal Vertical Migration by Marine Organisms on Marine Biogeochemistry. Global Biogeochemical Cycles 32:1622–1643.

Bailleul, F., J. Vacquie-Garcia, and C. Guinet. 2015. Dissolved Oxygen Sensor in Animal-Borne Instruments: An Innovation for Monitoring the Health of Oceans and Investigating the Functioning of Marine Ecosystems. PLOS ONE 10:e0132681.

Barton, A. D., A. J. Irwin, Z. V. Finkel, and C. A. Stock. 2016. Anthropogenic climate change drives shift and shuffle in North Atlantic phytoplankton communities. Proceedings of the National Academy of Sciences 113:2964–2969.

Bayle, S., P. Monestiez, C. Guinet, and D. Nerini. 2015. Moving toward finer scales in oceanography: Predictive linear functional model of Chlorophyll a profile from light data. Progress in Oceanography 134:221–231.

Béhagle, N., C. Cotté, A. Lebourges-Dhaussy, G. Roudaut, G. Duhamel, P. Brehmer, E. Josse, and Y. Cherel. 2017. Acoustic distribution of discriminated micronektonic organisms from a bi-frequency processing: The case study of eastern Kerguelen oceanic waters. Progress in Oceanography 156:276–289.

Béhagle, N., C. Cotté, T. E. Ryan, O. Gauthier, G. Roudaut, P. Brehmer, E. Josse, and Y. Cherel. 2016. Acoustic micronektonic distribution is structured by macroscale oceanographic processes across 20–50°S latitudes in the South-Western Indian Ocean. Deep Sea Research Part I: Oceanographic Research Papers 110:20–32.

Behrenfeld, M. J., P. Gaube, A. Della Penna, R. T. O'Malley, W. J. Burt, Y. Hu, P. S. Bontempi, D. K. Steinberg, E. S. Boss, D. A. Siegel, C. A. Hostetler, P. D. Tortell, and S. C. Doney. 2019. Global satellite-observed daily vertical migrations of ocean animals. Nature 576:257–261.

Belcher, A., C. Manno, P. Ward, S. Henson, R. Sanders, and G. Tarling. 2017. Copepod faecal pellet transfer through the meso- and bathypelagic layers in the Southern Ocean in spring. Biogeosciences 14:1511–1525.

Bianchi, D., and K. A. S. Mislan. 2016. Global patterns of diel vertical migration times and velocities from acoustic data: Global patterns of diel vertical migration. Limnology and Oceanography 61:353–364.

Biuw, M., L. Boehme, C. Guinet, M. Hindell, D. Costa, J.-B. Charrassin, F. Roquet, F. Bailleul, M. Meredith, S. Thorpe, Y. Tremblay, B. McDonald, Y.-H. Park, S. R. Rintoul, N. Bindoff, M. Goebel, D. Crocker, P. Lovell, J. Nicholson, F. Monks, and M. A. Fedak. 2007. Variations in behavior and condition of a Southern Ocean top predator in relation to in situ oceanographic conditions. Proceedings of the National Academy of Sciences 104:13705–13710.

Blain, S., B. Quéguiner, L. Armand, S. Belviso, B. Bombled, L. Bopp, A. Bowie, C. Brunet, C. Brussaard, F. Carlotti, U. Christaki, A. Corbière, I. Durand, F. Ebersbach, J.-L. Fuda, N. Garcia, L. Gerringa, B. Griffiths, C. Guigue, C. Guillerm, S. Jacquet, C. Jeandel, P. Laan, D. Lefèvre, C. Lo Monaco, A. Malits, J. Mosseri, I. Obernosterer, Y.-H. Park, M. Picheral, P. Pondaven, T. Remenyi, V.

671 Sandroni, G. Sarthou, N. Savoye, L. Scouarnec, M. Souhaut, D. Thuiller, K. Timmermans, T.
672 Trull, J. Uitz, P. van Beek, M. Veldhuis, D. Vincent, E. Viollier, L. Vong, and T. Wagener. 2007.
673 Effect of natural iron fertilization on carbon sequestration in the Southern Ocean. Nature
674 446:1070–1074.
675 Bost, C. A., C. Cotté, P. Terray, C. Barbraud, C. Bon, K. Delord, O. Gimenez, Y. Handrich, Y. Naito, C.
676 Guinet, and H. Weimerskirch. 2015. Large-scale climatic anomalies affect marine predator
677 foraging behaviour and demography. Nature Communications 6:8220.
678 Boyd, P. W., H. Claustre, M. Levy, D. A. Siegel, and T. Weber. 2019. Multi-faceted particle pumps
679 drive carbon sequestration in the ocean. Nature 568:327–335.
680 Brierley, A. S. 2014. Diel vertical migration. Current Biology 24:R1074–R1076.
681 Buesseler, K. O., and P. W. Boyd. 2009. Shedding light on processes that control particle export and
682 flux attenuation in the twilight zone of the open ocean. Limnology and Oceanography
683 54:1210–1232.
684 Buesseler, K. O., C. H. Lamborg, P. W. Boyd, P. J. Lam, T. W. Trull, R. R. Bidigare, J. K. B. Bishop, K. L.
685 Casciotti, F. Dehairs, M. Elskens, M. Honda, D. M. Karl, D. A. Siegel, M. W. Silver, D. K.
686 Steinberg, J. Valdes, B. V. Mooy, and S. Wilson. 2007. Revisiting Carbon Flux Through the
687 Ocean's Twilight Zone. Science 316:567–570.
688 Burwen, D. L., S. J. Fleischman, J. D. Miller, and M. E. Jensen. 2003. Time-based signal characteristics
689 as predictors of fish size and species for a side-looking hydroacoustic application in a river.
690 ICES Journal of Marine Science 60:662–668.
691 Carlotti, F., D. Thibault-Botha, A. Nowaczyk, and D. Lefèvre. 2008. Zooplankton community structure,
692 biomass and role in carbon fluxes during the second half of a phytoplankton bloom in the
693 eastern sector of the Kerguelen Shelf (January–February 2005). Deep Sea Research Part II:
694 Topical Studies in Oceanography 55:720–733.

695 Carter, L., I. N. McCave, and M. J. M. Williams. 2008. Chapter 4 Circulation and Water Masses of the
696 Southern Ocean: A Review. Pages 85–114 *in* F. Florindo and M. Siegert, editors.
697 Developments in Earth and Environmental Sciences. Elsevier.
698 Cavan, E. L., A. Belcher, A. Atkinson, S. L. Hill, S. Kawaguchi, S. McCormack, B. Meyer, S. Nicol, L.
699 Ratnarajah, K. Schmidt, D. K. Steinberg, G. A. Tarling, and P. W. Boyd. 2019a. The importance
700 of Antarctic krill in biogeochemical cycles. Nature Communications 10.
701 Cavan, E. L., E. C. Laurenceau-Cornec, M. Bressac, and P. W. Boyd. 2019b. Exploring the ecology of
702 the mesopelagic biological pump. Progress in Oceanography 176:102125.
703 Cavan, E. L., F. A. C. Le Moigne, A. J. Poulton, G. A. Tarling, P. Ward, C. J. Daniels, G. M. Fragoso, and
704 R. J. Sanders. 2015. Attenuation of particulate organic carbon flux in the Scotia Sea, Southern
705 Ocean, is controlled by zooplankton fecal pellets. Geophysical Research Letters 42:821–830.
706 Cepeda, G. D., B. Temperoni, M. E. Sabatini, M. D. Viñas, C. M. Derisio, B. A. Santos, J. C. Antacli, and
707 L. N. Padovani. 2018. Zooplankton Communities of the Argentine Continental Shelf (SW
708 Atlantic, ca. 34°–55°S), An Overview. Pages 171–199 *in* M. S. Hoffmeyer, M. E. Sabatini, F. P.
709 Brandini, D. L. Calliari, and N. H. Santinelli, editors. Plankton Ecology of the Southwestern
710 Atlantic. Springer International Publishing, Cham.
711 Chapman, C. C., M.-A. Lea, A. Meyer, J.-B. Sallée, and M. Hindell. 2020. Defining Southern Ocean
712 fronts and their influence on biological and physical processes in a changing climate. Nature
713 Climate Change 10:209–219.
714 Cherel, Y., S. Ducatez, C. Fontaine, P. Richard, and C. Guinet. 2008. Stable isotopes reveal the trophic
715 position and mesopelagic fish diet of female southern elephant seals breeding on the
716 Kerguelen Islands. Marine Ecology Progress Series 370:239–247.
717 Conroy, J. A., D. K. Steinberg, P. S. Thibodeau, and O. Schofield. 2020. Zooplankton diel vertical
718 migration during Antarctic summer. Deep Sea Research Part I: Oceanographic Research
719 Papers 162:103324.

720 Cotté, C., F. d'Ovidio, A.-C. Dragon, C. Guinet, and M. Lévy. 2015. Flexible preference of southern
721 elephant seals for distinct mesoscale features within the Antarctic Circumpolar Current.
722 Progress in Oceanography 131:46–58.
723 Cuzin-Roudy, J., J. Irisson, F. Penot, S. Kawaguchi, and C. Vallet. 2014. Southern Ocean Euphausiids.
724 Biogeographic Atlas Southern Ocean:510.
725 Daneri, G., and A. Carlini. 2002. Fish prey of southern elephant seals, Mirounga leonina, at King
726 George Island. Polar Biology 25:739–743.
727 Davison, P. C., J. A. Koslow, and R. J. Kloser. 2015. Acoustic biomass estimation of mesopelagic fish:
728 backscattering from individuals, populations, and communities. ICES Journal of Marine
729 Science 72:1413–1424.
730 Della Penna, A., S. De Monte, E. Kestenare, C. Guinet, and F. d'Ovidio. 2015. Quasi-planktonic
731 behavior of foraging top marine predators. Scientific Reports 5.
732 DeVries, T. 2014. The oceanic anthropogenic CO_2 sink: Storage, air-sea fluxes, and transports over
733 the industrial era. Global Biogeochemical Cycles 28:631–647.
734 Dornan, T., S. Fielding, R. A. Saunders, and M. J. Genner. 2019. Swimbladder morphology masks
735 Southern Ocean mesopelagic fish biomass. Proceedings of the Royal Society B: Biological
736 Sciences 286:20190353.
737 Dragon, A.-C., P. Monestiez, A. Bar-Hen, and C. Guinet. 2010. Linking foraging behaviour to physical
738 oceanographic structures: Southern elephant seals and mesoscale eddies east of Kerguelen
739 Islands. Progress in Oceanography 87:61–71.
740 Escobar-Flores, P. C., Y. Ladroit, and R. L. O'Driscoll. 2019. Acoustic Assessment of the Micronekton
741 Community on the Chatham Rise, New Zealand, Using a Semi-Automated Approach.
742 Frontiers in Marine Science 6.
743 Escobar-Flores, P. C., R. L. O'Driscoll, and J. C. Montgomery. 2018. Predicting distribution and relative
744 abundance of mid-trophic level organisms using oceanographic parameters and acoustic
745 backscatter. Marine Ecology Progress Series 592:37–56.

Fay, A. R., and G. A. McKinley. 2014. Global open-ocean biomes: mean and temporal variability. Earth System Science Data 6:273–284.

Fedak M. 2004. Marine animals as platforms for oceanographic sampling: a “win/win” situation for biology and operational oceanography 58:133–147.

Fielding, S., J. L. Watkins, P. N. Trathan, P. Enderlein, C. M. Waluda, G. Stowasser, G. A. Tarling, and E. J. Murphy. 2014. Interannual variability in Antarctic krill (Euphausia superba) density at South Georgia, Southern Ocean: 1997–2013. ICES Journal of Marine Science 71:2578–2588.

Godet, C., M. Robuchon, B. Leroy, C. Cotté, A. Baudena, O. Da Silva, S. Fabri-Ruiz, C. Lo Monaco, S. Sergi, and P. Koubbi. 2020. Matching zooplankton abundance and environment in the South Indian Ocean and Southern Ocean. Deep Sea Research Part I: Oceanographic Research Papers 163:103347.

Goulet, P., C. Guinet, C. Campagna, J. Campagna, P. L. Tyack, and M. Johnson. 2020. Flash and grab: deep-diving southern elephant seals trigger anti-predator flashes in bioluminescent prey. The Journal of Experimental Biology 223:jeb222810.

Goulet, P., C. Guinet, R. Swift, P. T. Madsen, and M. Johnson. 2019. A miniature biomimetic sonar and movement tag to study the biotic environment and predator-prey interactions in aquatic animals. Deep Sea Research Part I: Oceanographic Research Papers 148:1–11.

Guinet, C., J. Vacquié-Garcia, B. Picard, G. Bessigneul, Y. Lebras, A. Dragon, M. Viviant, J. Arnould, and F. Bailleul. 2014. Southern elephant seal foraging success in relation to temperature and light conditions: insight into prey distribution. Marine Ecology Progress Series 499:285–301.

Haëntjens, N., A. Della Penna, N. Briggs, L. Karp-Boss, P. Gaube, H. Claustre, and E. Boss. 2020. Detecting Mesopelagic Organisms Using Biogeochemical-Argo Floats. Geophysical Research Letters 47.

Handegard, N. O., D. A. Demer, R. Kloser, P. Lehodey, O. Maury, and Y. Simard. 2009. Toward a Global Ocean Ecosystem Mid-trophic Automatic Acoustic Sampler (MAAS). 8 s.

771 Harcourt, R., A. M. M. Sequeira, X. Zhang, F. Roquet, K. Komatsu, M. Heupel, C. McMahon, F.
772 Whoriskey, M. Meekan, G. Carroll, S. Brodie, C. Simpfendorfer, M. Hindell, I. Jonsen, D. P.
773 Costa, B. Block, M. Muelbert, B. Woodward, M. Weise, K. Aarestrup, M. Biuw, L. Boehme, S.
774 J. Bograd, D. Cazau, J.-B. Charrassin, S. J. Cooke, P. Cowley, P. J. N. de Bruyn, T. Jeanniard du
775 Dot, C. Duarte, V. M. Eguíluz, L. C. Ferreira, J. Fernández-Gracia, K. Goetz, Y. Goto, C. Guinet,
776 M. Hammill, G. C. Hays, E. L. Hazen, L. A. Hückstädt, C. Huveneers, S. Iverson, S. A. Jaaman, K.
777 Kittiwattanawong, K. M. Kovacs, C. Lydersen, T. Moltmann, M. Naruoka, L. Phillips, B. Picard,
778 N. Queiroz, G. Reverdin, K. Sato, D. W. Sims, E. B. Thorstad, M. Thums, A. M. Treasure, A. W.
779 Trites, G. D. Williams, Y. Yonehara, and M. A. Fedak. 2019. Animal-Borne Telemetry: An
780 Integral Component of the Ocean Observing Toolkit. Frontiers in Marine Science 6.
781 Hays, G. C. 2003. A review of the adaptive significance and ecosystem consequences of zooplankton
782 diel vertical migrations. Pages 163–170 *in* M. B. Jones, A. Ingólfsson, E. Ólafsson, G. V.
783 Helgason, K. Gunnarsson, and J. Svavarsson, editors. Migrations and Dispersal of Marine
784 Organisms. Springer Netherlands, Dordrecht.
785 Heneghan, R. F., J. D. Everett, J. L. Blanchard, and A. J. Richardson. 2016. Zooplankton Are Not Fish:
786 Improving Zooplankton Realism in Size-Spectrum Models Mediates Energy Transfer in Food
787 Webs. Frontiers in Marine Science 3.
788 Hernández-León, S., R. Koppelmann, E. Fraile-Nuez, A. Bode, C. Mompeán, X. Irigoien, M. P. Olivar, F.
789 Echevarría, M. L. Fernández de Puelles, J. I. González-Gordillo, A. Cózar, J. L. Acuña, S. Agustí,
790 and C. M. Duarte. 2020. Large deep-sea zooplankton biomass mirrors primary production in
791 the global ocean. Nature Communications 11:6048.
792 Hernández-León, S., M. P. Olivar, M. L. Fernández de Puelles, A. Bode, A. Castellón, C. López-Pérez, V.
793 M. Tuset, and J. I. González-Gordillo. 2019. Zooplankton and Micronekton Active Flux Across
794 the Tropical and Subtropical Atlantic Ocean. Frontiers in Marine Science 6.
795 Hidalgo, M., and H. I. Browman. 2019. Developing the knowledge base needed to sustainably
796 manage mesopelagic resources. ICES Journal of Marine Science 76:609–615.

797 Hindell, M. A., C. R. McMahon, M. N. Bester, L. Boehme, D. Costa, M. A. Fedak, C. Guinet, L. Herraiz-
798 Borreguero, R. G. Harcourt, L. Huckstadt, K. M. Kovacs, C. Lydersen, T. McIntyre, M.
799 Muelbert, T. Patterson, F. Roquet, G. Williams, and J. Charrassin. 2016. Circumpolar habitat
800 use in the southern elephant seal: implications for foraging success and population
801 trajectories. Ecosphere 7.
802 Irigoien, X., T. A. Klevjer, A. Røstad, U. Martinez, G. Boyra, J. L. Acuña, A. Bode, F. Echevarria, J. I.
803 Gonzalez-Gordillo, S. Hernandez-Leon, S. Agusti, D. L. Aksnes, C. M. Duarte, and S. Kaartvedt.
804 2014. Large mesopelagic fishes biomass and trophic efficiency in the open ocean. Nature
805 Communications 5.
806 Jouma'a, J., Y. Le Bras, G. Richard, J. Vacquié-Garcia, B. Picard, N. El Ksabi, and C. Guinet. 2016.
807 Adjustment of diving behaviour with prey encounters and body condition in a deep diving
808 predator: the Southern Elephant Seal. Functional Ecology 30:636–648.
809 Kaartvedt, S., A. Staby, and D. Aksnes. 2012. Efficient trawl avoidance by mesopelagic fishes causes
810 large underestimation of their biomass. Marine Ecology Progress Series 456:1–6.
811 Kloke, J. D., and J. W. McKean. 2012. Rfit: Rank-based estimation for linear models. The R journal
812 4:57–64.
813 Kloser, R. J., T. E. Ryan, G. Keith, and L. Gershwin. 2016. Deep-scattering layer, gas-bladder density,
814 and size estimates using a two-frequency acoustic and optical probe. ICES Journal of Marine
815 Science 73:2037–2048.
816 Kloser, R. J., T. E. Ryan, J. W. Young, and M. E. Lewis. 2009. Acoustic observations of micronekton fish
817 on the scale of an ocean basin: potential and challenges. ICES Journal of Marine Science
818 66:998–1006.
819 Koubbi, P., C. Guinet, N. Alloncle, N. Ameziane, C. Azam, A. Baudena, C. Bost, R. Causse, C. Chazeau,
820 and G. Coste. 2016. Ecoregionalisation of the Kerguelen and Crozet islands oceanic zone. Part
821 I: Introduction and Kerguelen oceanic zone. CCAMLR Document WG-EMM-16/43.

822 Latasa, M., J. Henjes, R. Scharek, P. Assmy, R. Röttgers, and V. Smetacek. 2014. Progressive
823 decoupling between phytoplankton growth and microzooplankton grazing during an iron-
824 induced phytoplankton bloom in the Southern Ocean (EIFEX). Marine Ecology Progress Series
825 513:39–50.
826 Laurenceau-Cornec, E. C., T. W. Trull, D. M. Davies, S. G. Bray, J. Doran, F. Planchon, F. Carlotti, M.-P.
827 Jouandet, A.-J. Cavagna, A. M. Waite, and S. Blain. 2015a. The relative importance of
828 phytoplankton aggregates and zooplankton fecal pellets to carbon export: insights from free-
829 drifting sediment trap deployments in naturally iron-fertilised waters near the Kerguelen
830 Plateau. Biogeosciences 12:1007–1027.
831 Laurenceau-Cornec, E. C., T. W. Trull, D. M. Davies, C. L. D. L. Rocha, and S. Blain. 2015b.
832 Phytoplankton morphology controls on marine snow sinking velocity. Marine Ecology
833 Progress Series 520:35–56.
834 Le Bras, Y., J. Jouma'a, B. Picard, and C. Guinet. 2016. How Elephant Seals (Mirounga leonina) Adjust
835 Their Fine Scale Horizontal Movement and Diving Behaviour in Relation to Prey Encounter
836 Rate. PLOS ONE 11:e0167226.
837 Le Moigne, F. A. C. L., S. A. Henson, E. Cavan, C. Georges, K. Pabortsava, E. P. Achterberg, E. Ceballos-
838 Romero, M. Zubkov, and R. J. Sanders. 2016. What causes the inverse relationship between
839 primary production and export efficiency in the Southern Ocean? Geophysical Research
840 Letters 43:4457–4466.
841 Leblanc, K., A. Lafond, V. Cornet, J. Legras, B. Marie, and B. Quéguiner. this issue. Leblanc, K., A.
842 Lafond, A., V. Cornet, J. Legras, B. Marie, B. Quéguiner this issue). Deep particle stocks
843 following the summer bloom around the Kerguelen islands: insights into diatoms
844 physiological state, community structure and mortality modes. Journal of Marine Systems
845 (under revision) This issue.
846 Longhurst, A. R. 2010. Ecological geography of the sea. Elsevier.

847 Lutz, V., V. Segura, A. Dogliotti, V. Tavano, F. P. Brandini, D. L. Calliari, A. M. Ciotti, V. F. Villafañe, I. R.
848 Schloss, F. M. P. S. Corrêa, H. Benavides, and D. V. Cantonnet. 2018. Overview on Primary
849 Production in the Southwestern Atlantic. Pages 101–126 *in* M. S. Hoffmeyer, M. E. Sabatini,
850 F. P. Brandini, D. L. Calliari, and N. H. Santinelli, editors. Plankton Ecology of the
851 Southwestern Atlantic: From the Subtropical to the Subantarctic Realm. Springer
852 International Publishing, Cham.
853 Manno, C., S. Fielding, G. Stowasser, E. J. Murphy, S. E. Thorpe, and G. A. Tarling. 2020. Continuous
854 moulting by Antarctic krill drives major pulses of carbon export in the north Scotia Sea,
855 Southern Ocean. Nature Communications 11:6051.
856 McMahon, C. R., I. C. Field, C. J. A. Bradshaw, G. C. White, and M. A. Hindell. 2008. Tracking and
857 data–logging devices attached to elephant seals do not affect individual mass gain or
858 survival. Journal of Experimental Marine Biology and Ecology 360:71–77.
859 McMahon, C. R., M. A. Hindell, J.-B. Charrassin, S. Corney, C. Guinet, R. Harcourt, I. Jonsen, R.
860 Trebilco, G. Williams, and S. Bestley. 2019. Finding mesopelagic prey in a changing Southern
861 Ocean. Scientific Reports 9:19013.
862 Montes-Hugo, M., S. C. Doney, H. W. Ducklow, W. Fraser, D. Martinson, S. E. Stammerjohn, and O.
863 Schofield. 2009. Recent Changes in Phytoplankton Communities Associated with Rapid
864 Regional Climate Change Along the Western Antarctic Peninsula. Science 323:1470–1473.
865 Murtagh, F., and P. Legendre. 2014. Ward's Hierarchical Agglomerative Clustering Method: Which
866 Algorithms Implement Ward's Criterion? Journal of Classification 31:274–295.
867 Naito, Y., D. P. Costa, T. Adachi, P. W. Robinson, M. Fowler, and A. Takahashi. 2013. Unravelling the
868 mysteries of a mesopelagic diet: a large apex predator specializes on small prey. Functional
869 Ecology 27:710–717.
870
871 Nerini, D., and B. Ghattas. 2007. Classifying densities using functional regression trees: Applications
872 in oceanology. Computational Statistics & Data Analysis 51:4984–4993.

873 Pauthenet, E., F. Roquet, G. Madec, and D. Nerini. 2017. A Linear Decomposition of the Southern
874 Ocean Thermohaline Structure. Journal of Physical Oceanography 47:29–47.
875 Pinti, J., and A. W. Visser. 2018. Predator-Prey Games in Multiple Habitats Reveal Mixed Strategies in
876 Diel Vertical Migration. The American Naturalist 193:E65–E77.
877 Pollard, R. T., I. Salter, R. J. Sanders, M. I. Lucas, C. M. Moore, R. A. Mills, P. J. Statham, J. T. Allen, A.
878 R. Baker, D. C. E. Bakker, M. A. Charette, S. Fielding, G. R. Fones, M. French, A. E. Hickman, R.
879 J. Holland, J. A. Hughes, T. D. Jickells, R. S. Lampitt, P. J. Morris, F. H. Nédélec, M. Nielsdóttir,
880 H. Planquette, E. E. Popova, A. J. Poulton, J. F. Read, S. Seeyave, T. Smith, M. Stinchcombe, S.
881 Taylor, S. Thomalla, H. J. Venables, R. Williamson, and M. V. Zubkov. 2009. Southern Ocean
882 deep-water carbon export enhanced by natural iron fertilization. Nature 457:577–580.
883 Proud, R., M. J. Cox, C. L. Guen, and A. S. Brierley. 2018. Fine-scale depth structure of pelagic
884 communities throughout the global ocean based on acoustic sound scattering layers. Marine
885 Ecology Progress Series 598:35–48.
886 Proud, R., N. O. Handegard, R. J. Kloser, M. J. Cox, and A. S. Brierley. 2019. From siphonophores to
887 deep scattering layers: uncertainty ranges for the estimation of global mesopelagic fish
888 biomass. ICES Journal of Marine Science 76:718–733.
889 Ramsay, J., and B. Silverman. 2005. Principal components analysis for functional data. Functional
890 data analysis:147–172.
891 Rembauville, M., I. Salter, N. Leblond, A. Gueneugues, and S. Blain. 2015. Export fluxes in a naturally
892 iron-fertilized area of the Southern Ocean – Part 1: Seasonal dynamics of particulate organic
893 carbon export from a moored sediment trap. Biogeosciences 12:3153–3170.
894 Reygondeau, G., L. Guidi, G. Beaugrand, S. A. Henson, P. Koubbi, B. R. MacKenzie, T. T. Sutton, M.
895 Fioroni, and O. Maury. 2018. Global biogeochemical provinces of the mesopelagic zone.
896 Journal of Biogeography 45:500–514.

Rivière, P., T. Jaud, L. Siegelman, P. Klein, C. Cotté, J. Le Sommer, G. Dencausse, and C. Guinet. 2019. Sub-mesoscale fronts modify elephant seals foraging behavior. Limnology and Oceanography Letters 4:193–204.

Robinson, J., E. E. Popova, M. A. Srokosz, and A. Yool. 2016. A tale of three islands: Downstream natural iron fertilization in the Southern Ocean. Journal of Geophysical Research: Oceans 121:3350–3371.

Roquet, F., Y.-H. Park, C. Guinet, F. Bailleul, and J.-B. Charrassin. 2009. Observations of the Fawn Trough Current over the Kerguelen Plateau from instrumented elephant seals. Journal of Marine Systems 78:377–393.

Roquet, F., C. Wunsch, G. Forget, P. Heimbach, C. Guinet, G. Reverdin, J.-B. Charrassin, F. Bailleul, D. P. Costa, L. A. Huckstadt, K. T. Goetz, K. M. Kovacs, C. Lydersen, M. Biuw, O. A. Nøst, H. Bornemann, J. Ploetz, M. N. Bester, T. McIntyre, M. C. Muelbert, M. A. Hindell, C. R. McMahon, G. Williams, R. Harcourt, I. C. Field, L. Chafik, K. W. Nicholls, L. Boehme, and M. A. Fedak. 2013. Estimates of the Southern Ocean general circulation improved by animal-borne instruments. Geophysical Research Letters 40:6176–6180.

Sallée, J., K. Speer, and R. Morrow. 2008. Southern Ocean fronts and their variability to climate modes. J. Clim 21:3020–3039.

Salter, I., A. E. S. Kemp, C. M. Moore, R. S. Lampitt, G. A. Wolff, and J. Holtvoeth. 2012. Diatom resting spore ecology drives enhanced carbon export from a naturally iron-fertilized bloom in the Southern Ocean. Global Biogeochemical Cycles 26.

Schallenberg, C., S. Bestley, A. Klocker, T. W. Trull, D. M. Davies, M. Gault-Ringold, R. Eriksen, N. P. Roden, S. G. Sander, M. Sumner, A. T. Townsend, P. van der Merwe, K. Westwood, K. Wuttig, and A. Bowie. 2018. Sustained Upwelling of Subsurface Iron Supplies Seasonally Persistent Phytoplankton Blooms Around the Southern Kerguelen Plateau, Southern Ocean. Journal of Geophysical Research: Oceans 123:5986–6003.

Sieburth, J. M., V. Smetacek, and J. Lenz. 1978. Pelagic ecosystem structure: Heterotrophic compartments of the plankton and their relationship to plankton size fractions 1. Limnology and Oceanography 23:1256–1263.

Siegelman, L., M. O'Toole, M. Flexas, P. Rivière, and P. Klein. 2019. Submesoscale ocean fronts act as biological hotspot for southern elephant seal. Scientific Reports 9.

Sims, D. W., V. J. Wearmouth, E. J. Southall, J. M. Hill, P. Moore, K. Rawlinson, N. Hutchinson, G. C. Budd, D. Righton, J. D. Metcalfe, J. P. Nash, and D. Morritt. 2006. Hunt warm, rest cool: bioenergetic strategy underlying diel vertical migration of a benthic shark. Journal of Animal Ecology 75:176–190.

St. John, M. A., A. Borja, G. Chust, M. Heath, I. Grigorov, P. Mariani, A. P. Martin, and R. S. Santos. 2016. A Dark Hole in Our Understanding of Marine Ecosystems and Their Services: Perspectives from the Mesopelagic Community. Frontiers in Marine Science 3.

Sutton, T. T. 2013. Vertical ecology of the pelagic ocean: classical patterns and new perspectives: vertical ecology of the pelagic ocean. Journal of Fish Biology 83:1508–1527.

Sydeman, W. J., E. Poloczanska, T. E. Reed, and S. A. Thompson. 2015. Climate change and marine vertebrates. Science 350:772–777.

Tarling, G. A., S. E. Thorpe, S. Fielding, T. Klevjer, A. Ryabov, and P. J. Somerfield. 2018. Varying depth and swarm dimensions of open-ocean Antarctic krill Euphausia superba Dana, 1850 (Euphausiacea) over diel cycles. Journal of Crustacean Biology 38:716–727.

Thompson, G. A., E. O. Dinofrio, and V. A. Alder. 2013. Structure, abundance and biomass size spectra of copepods and other zooplankton communities in upper waters of the Southwestern Atlantic Ocean during summer. Journal of Plankton Research 35:610–629.

Tran, T. K., L. Duforêt-Gaurier, V. Vantrepotte, D. S. F. Jorge, X. Mériaux, A. Cauvin, O. Fanton d'Andon, and H. Loisel. 2019. Deriving Particulate Organic Carbon in Coastal Waters from Remote Sensing: Inter-Comparison Exercise and Development of a Maximum Band-Ratio Approach. Remote Sensing 11:2849.

948 Turner, J. T. 2015. Zooplankton fecal pellets, marine snow, phytodetritus and the ocean's biological
949 pump. Progress in Oceanography 130:205–248.
950 Vacquié-Garcia, J., C. Guinet, C. Laurent, and F. Bailleul. 2015. Delineation of the southern elephant
951 seal's main foraging environments defined by temperature and light conditions. Deep Sea
952 Research Part II: Topical Studies in Oceanography 113:145–153.
953 Vacquié-Garcia, J., J. Mallefet, F. Bailleul, B. Picard, and C. Guinet. 2017. Marine Bioluminescence:
954 Measurement by a Classical Light Sensor and Related Foraging Behavior of a Deep Diving
955 Predator. Photochemistry and Photobiology 93:1312–1319.
956 Watanabe, H., T. Kubodera, M. Moku, and K. Kawaguchi. 2006. Diel vertical migration of squid in the
957 warm core ring and cold water masses in the transition region of the western North Pacific.
958 Marine Ecology Progress Series 315:187–197.
959 Watanabe, Y. Y., and A. Takahashi. 2013. Linking animal-borne video to accelerometers reveals prey
960 capture variability. Proceedings of the National Academy of Sciences 110:2199.
961 Wiebe, P. H., D. Chu, S. Kaartvedt, A. Hundt, W. Melle, E. Ona, and P. Batta-Lona. 2010. The acoustic
962 properties of Salpa thompsoni. ICES Journal of Marine Science 67:583–593.
963 Ydesen, K. S., D. M. Wisniewska, J. D. Hansen, K. Beedholm, M. Johnson, and P. T. Madsen. 2014.
964 What a jerk: prey engulfment revealed by high-rate, super-cranial accelerometry on a
965 harbour seal (Phoca vitulina). Journal of Experimental Biology 217:2239–2243.
966 Yoshino, K., A. Takahashi, T. Adachi, D. P. Costa, P. W. Robinson, S. H. Peterson, L. A. Hückstädt, R. R.
967 Holser, and Y. Naito. 2020. Acceleration-triggered animal-borne videos show a dominance of
968 fish in the diet of female northern elephant seals. Journal of Experimental Biology 223.
969
970

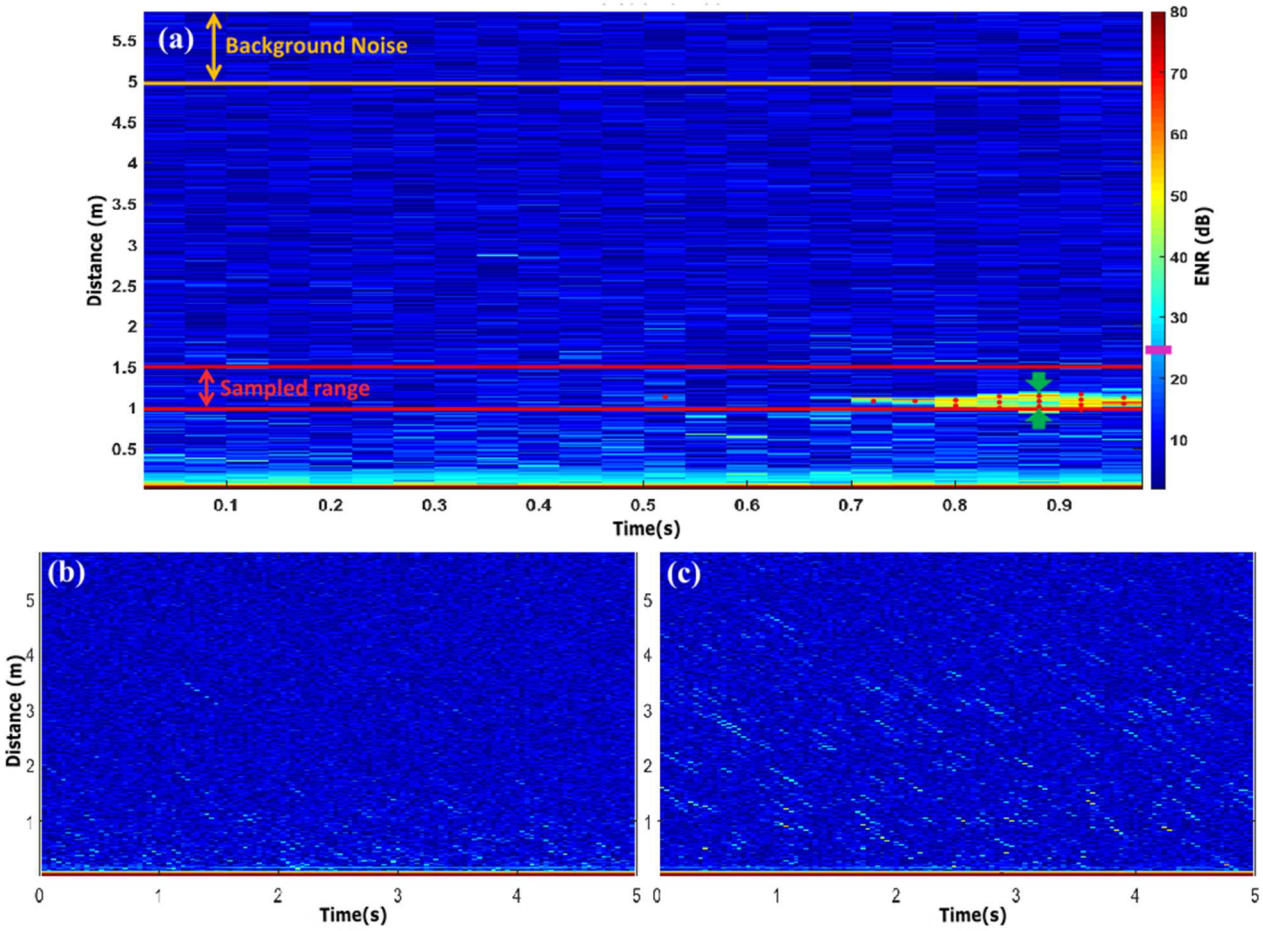

Figure 1: (a) Echogram with a schematic representation of the metrics calculations. Red lines mark the analysis range. The orange line shows the range used for Background Noise Level estimation. (b) Echogram from a regular area. (c) Echogram from the high-intensity signal region.

977

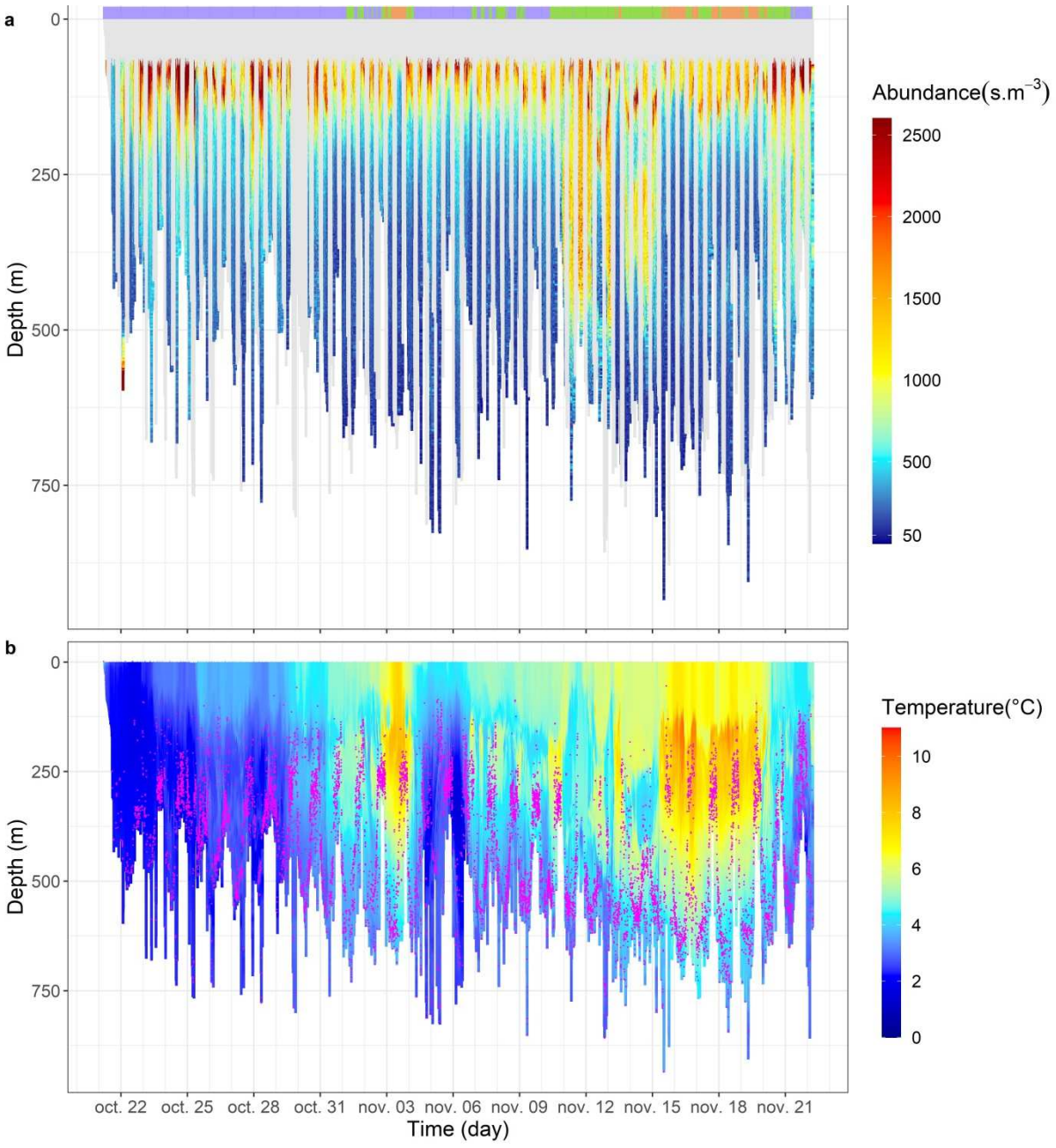

978

979 **Figure 2: (a) Time-depth series of scatterer abundance, expressed in scatterers.m^{-3}, detected by**
980 **the sonar tag on a seal tagged on Kerguelen Island (KER). The coloured rectangles above the**
981 **plot indicate the position of inferred water body types 1 (purple), 2 (green) and 3 (light orange).**
982 **(b) Water temperature profiles recorded by a tag on the same animal. Pink points indicate prey**
983 **capture attempts inferred from acceleration transients.**

984

985

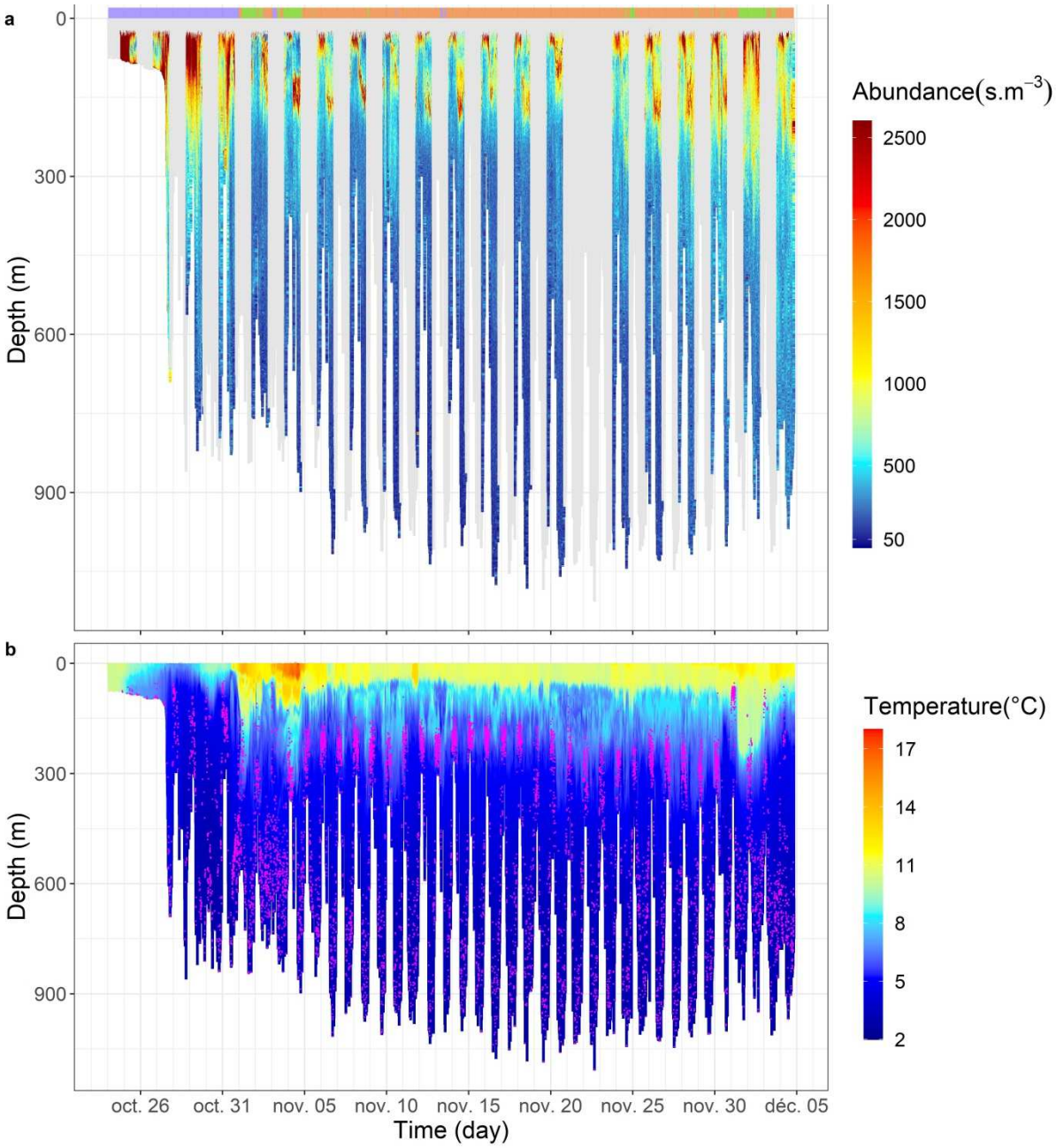

986

987 **Figure 3: (a) Time-depth series of scatterer abundance, expressed in scatterers.m^{-3}, detected by**
988 **the sonar tag on a seal tagged on Peninsula Valdes (PV). The coloured rectangles above the plot**
989 **indicate the position of inferred water body types 1 (purple), 2 (green) and 3 (light orange). (b)**
990 **Water temperature profiles recorded by a tag on the same animal. Pink points indicate prey**
991 **capture attempts inferred from acceleration transients. The colour scales have different ranges**
992 **than in Figure 2 to accommodate the differing conditions in this oceanographic region.**

993

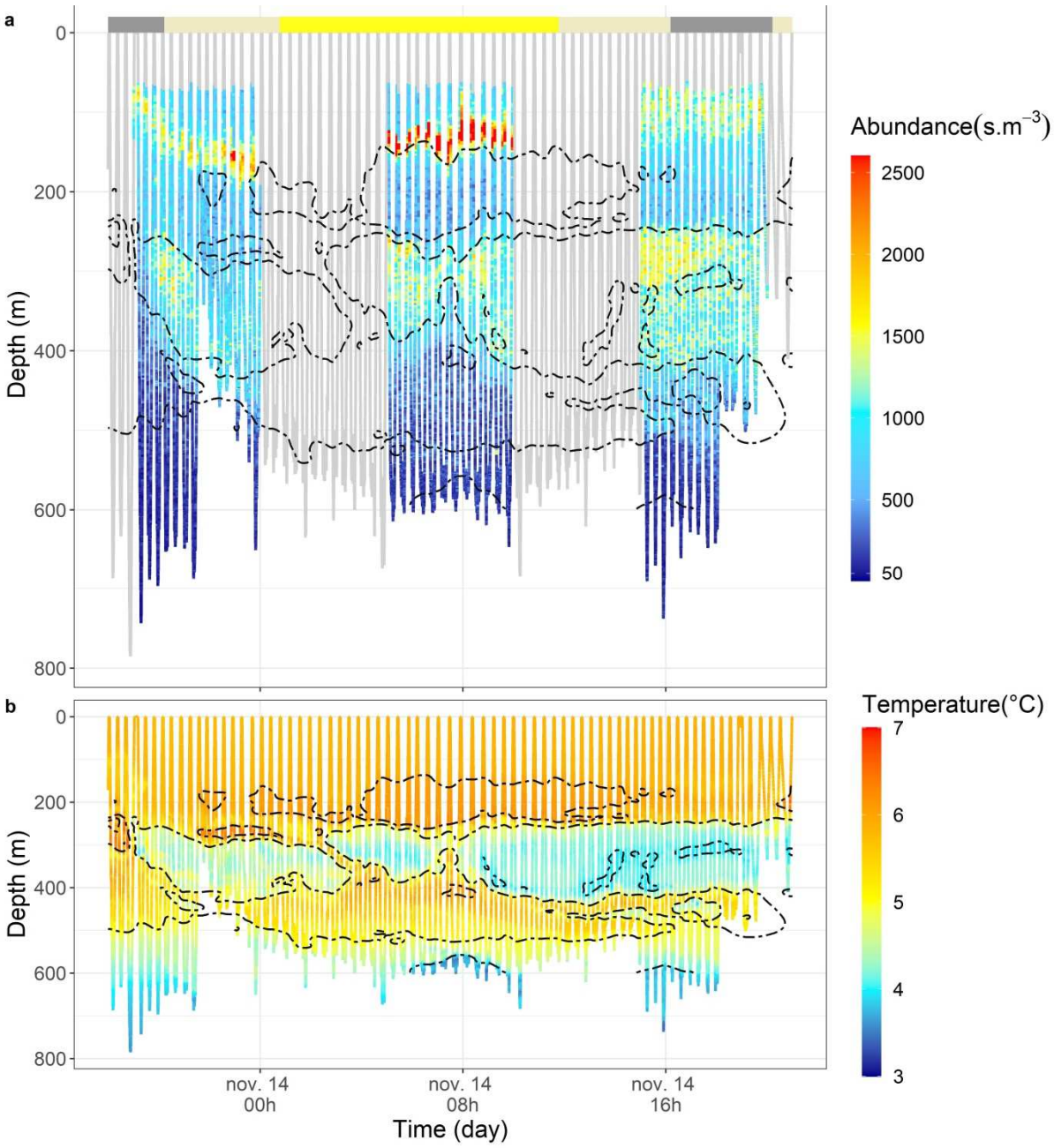

Figure 4: (a) Time-depth representation of the relative abundance of scatterers, expressed in scatterers.m^{-3}, detected by the sonar tag, zoomed over a one-day period for KER. The coloured rectangles represent the light angle with yellow and grey for day and night, respectively, and the shaded grey for twilight. The sonar was operated on a 5.5-hour on/off duty-cycle. (b) Temperature profiles, in °C for the same time interval. The dotted black lines in both plots represent the isotherms, with an increment of 1°C.

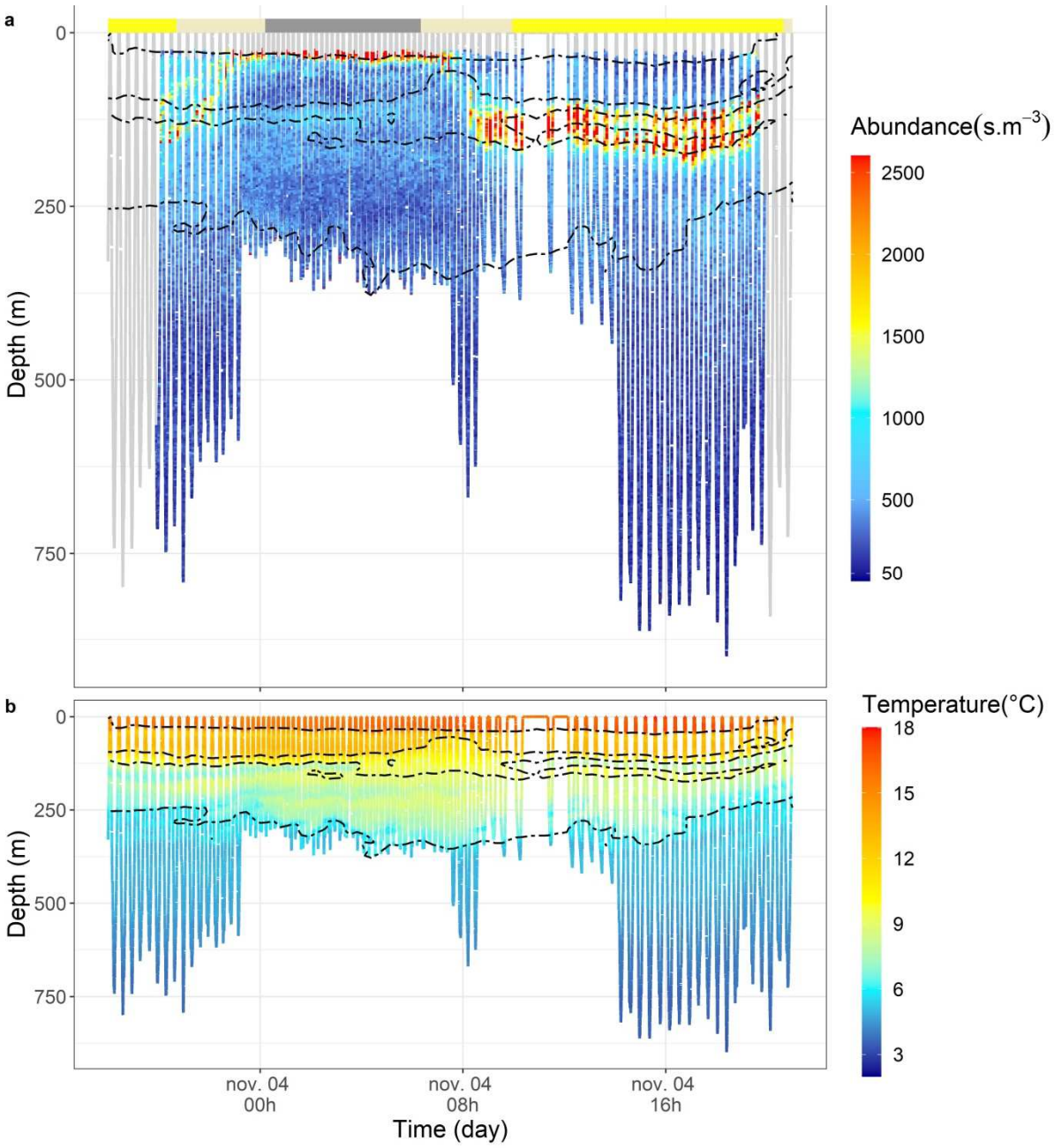

Figure 5: (a) Time-depth representation of the relative abundance of scatterers, expressed in scatterers.m^{-3}, detected by the sonar tag, zoomed over a one-day period for PV. The coloured rectangles represent the light angle with yellow and grey for day and night, respectively, and the shaded grey for twilight. The sonar was operated on a 12-hour on/off duty-cycle. (b) Temperature profiles, in °C for the same time interval. The dotted black line represents the isotherms, with an increment of 3°C.

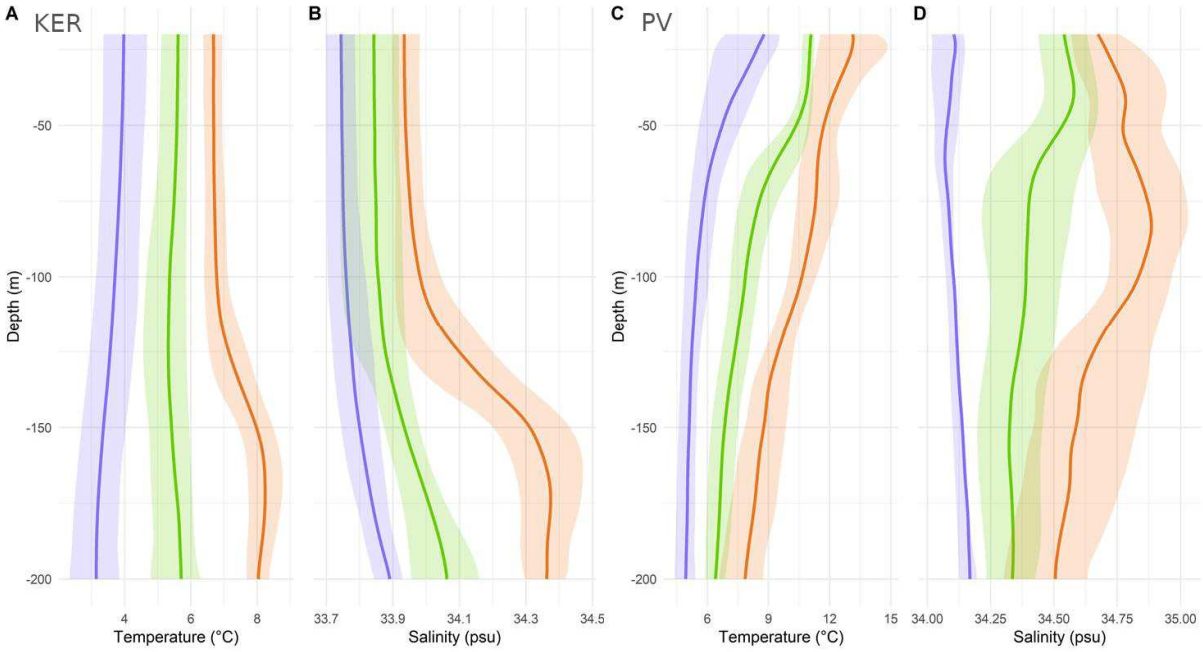

1010

1011 **Figure 6: Average temperature (A, C) and salinity (B, D) profiles of KER and PV datasets. The**
1012 **three clusters are shown in blue (cluster 1), green (cluster 2) and orange (cluster 3). For each**
1013 **profile, the envelopes are bounded by the first and last quartile and thus contain 50% of the**
1014 **profiles.**

1015

1016

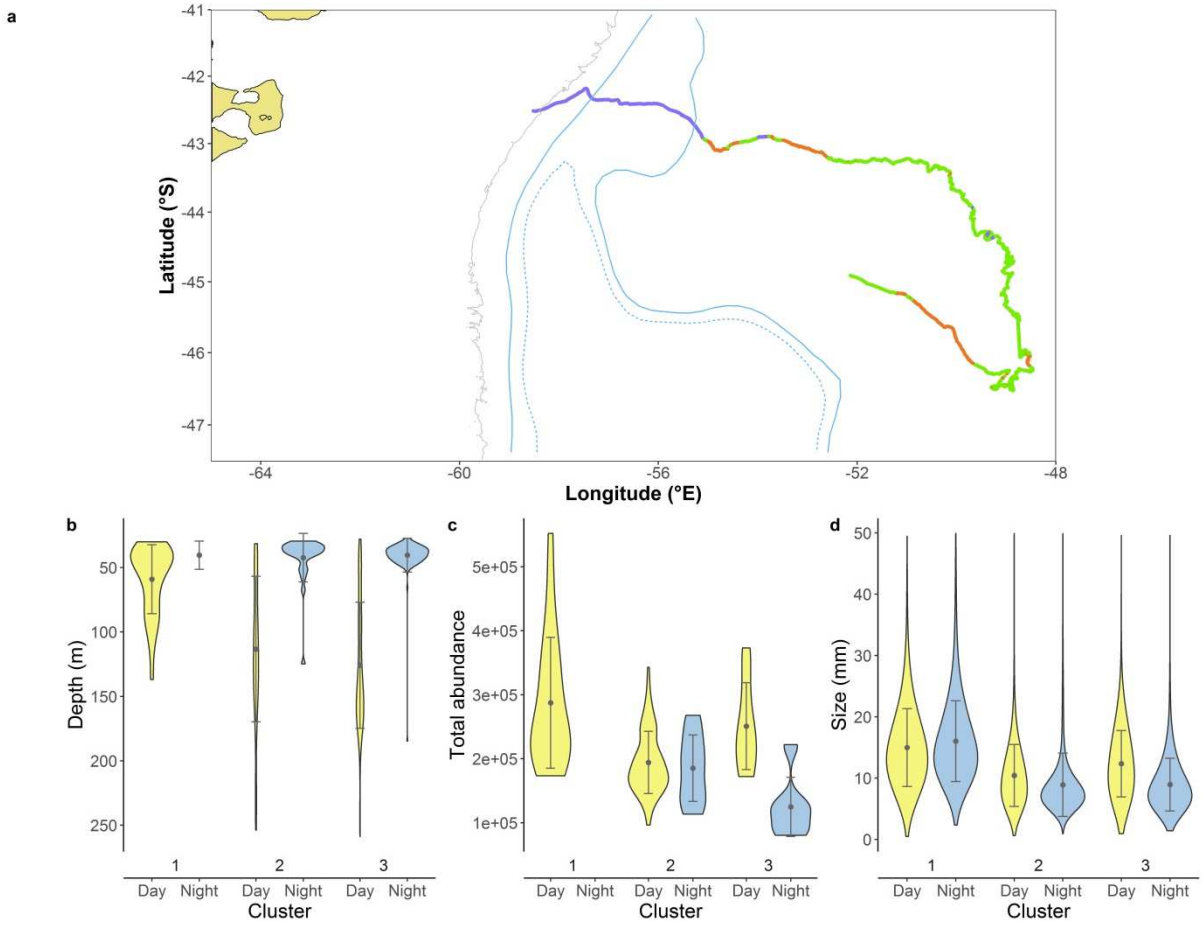

1017

1018 **Figure 7: (a) Track of the SES tagged on Peninsula Valdes during the interval recorded by the**
1019 **sonar tag (FPCA cluster colours as in Figure 6). The solid grey line shows the 1000 m isobath.**
1020 **Blue lines indicate the mean position of oceanic fronts over the study period, as given by the**
1021 **Centre for Topographic studies of the Ocean and Hydrosphere (see Sallée *et al.* 2008). Lower**
1022 **panels: (b) mean day (yellow) and night (blue) DVM depth (maximum abundance of profiles)**
1023 **for the 3 water clusters for the PV seal, (c) sum of the scatterers' abundances over the depth**
1024 **range 30-260 m (matching the vertical extent of the DVM depth for each cluster), (d) average**
1025 **scatterers' size distribution for each cluster. Grey dots and error bars respectively indicate the**
1026 **mean of each violin plot and the standard deviation.**

1027

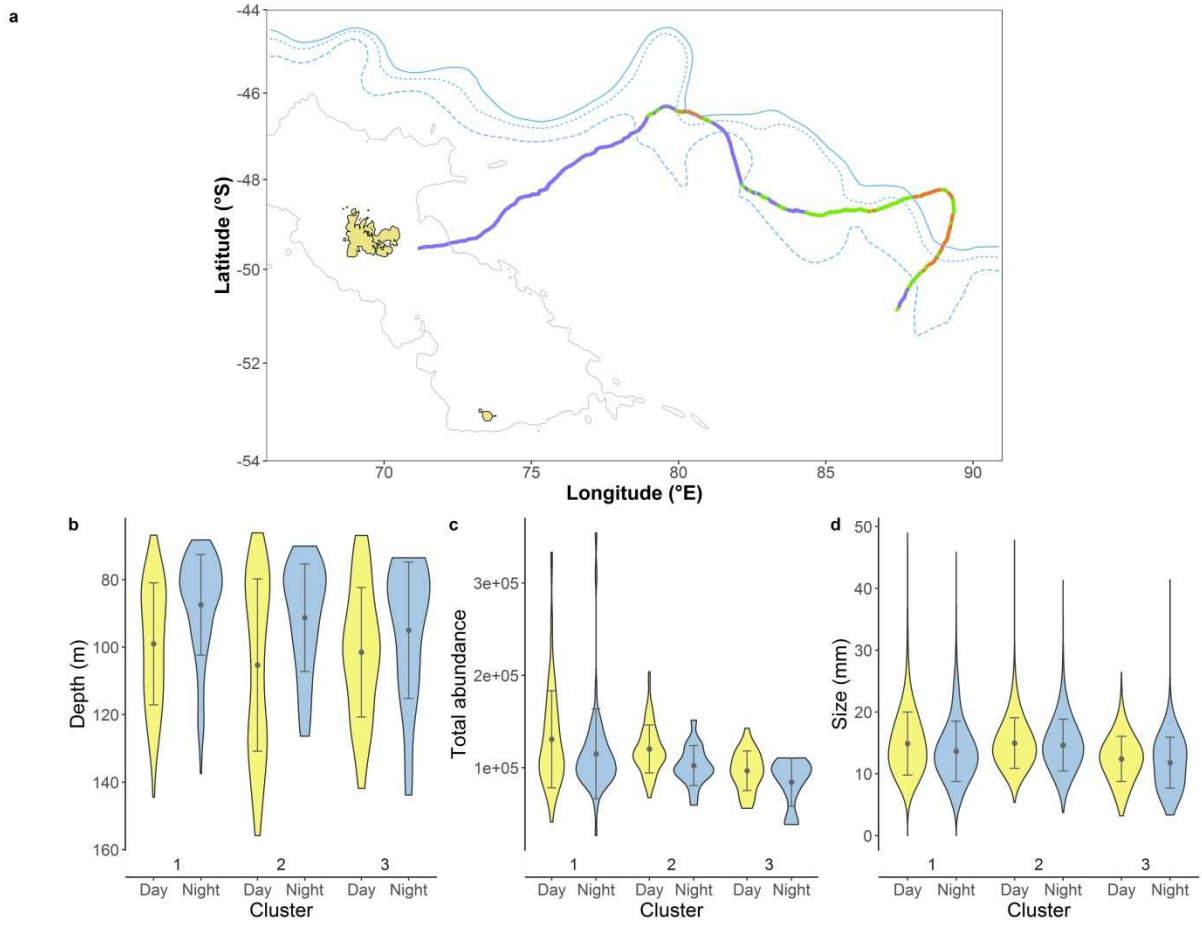

Figure 8: (a) Track of the SES tagged on Kerguelen Island during the interval recorded by the sonar tag (FPCA cluster colours as in Figure 6). The solid grey line shows the 1000 m isobath. Blue lines indicate the mean position of oceanic fronts over the study period, as given by the Centre for Topographic studies of the Ocean and Hydrosphere (see Sallée *et al.* 2008). Lower panels: (b) mean day (yellow) and night (blue) DVM depth (maximum abundance of profiles) for the 3 water clusters for the KER seal, (c) sum of the scatterers' abundances over the depth range 70-160 m (matching the vertical extent of the DVM depth for each cluster), (d) average scatterers' size distribution for each cluster. Grey dots and error bars respectively indicate the mean of each violin plot and the standard deviation.

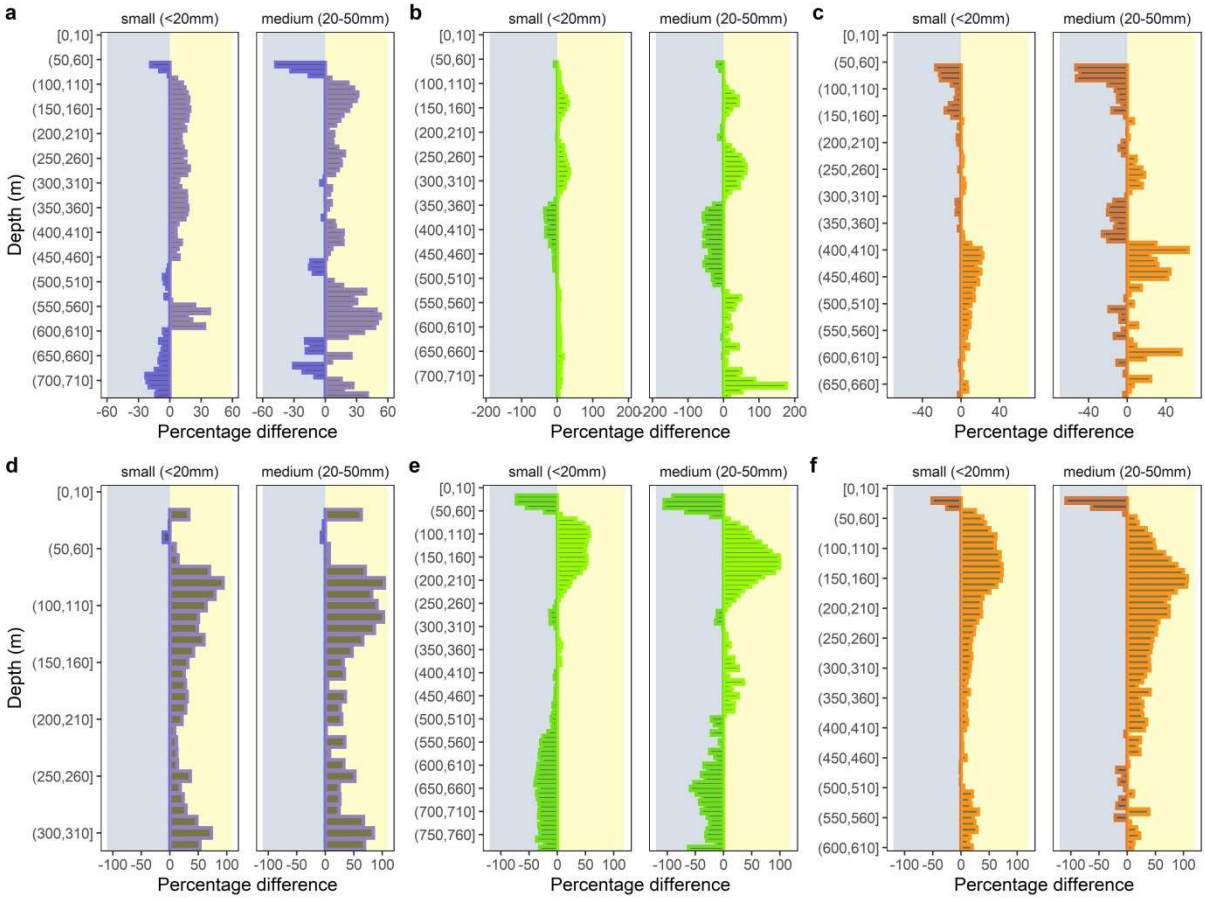

1039

1040 **Figure 9**: **Percentage difference, for small- (left) and medium- (right) size scatterers between day**
1041 **(yellow) and night (grey), calculated over 10-m depth bins, for the three water clusters (colours as**
1042 **in Figure 6) for KER (upper panel) and PV (lower panel). Positive values correspond to higher**
1043 **abundances during daytime than at night, and conversely a negative difference indicates higher**
1044 **abundances at night than during daytime for this depth bin.**

1045

1046

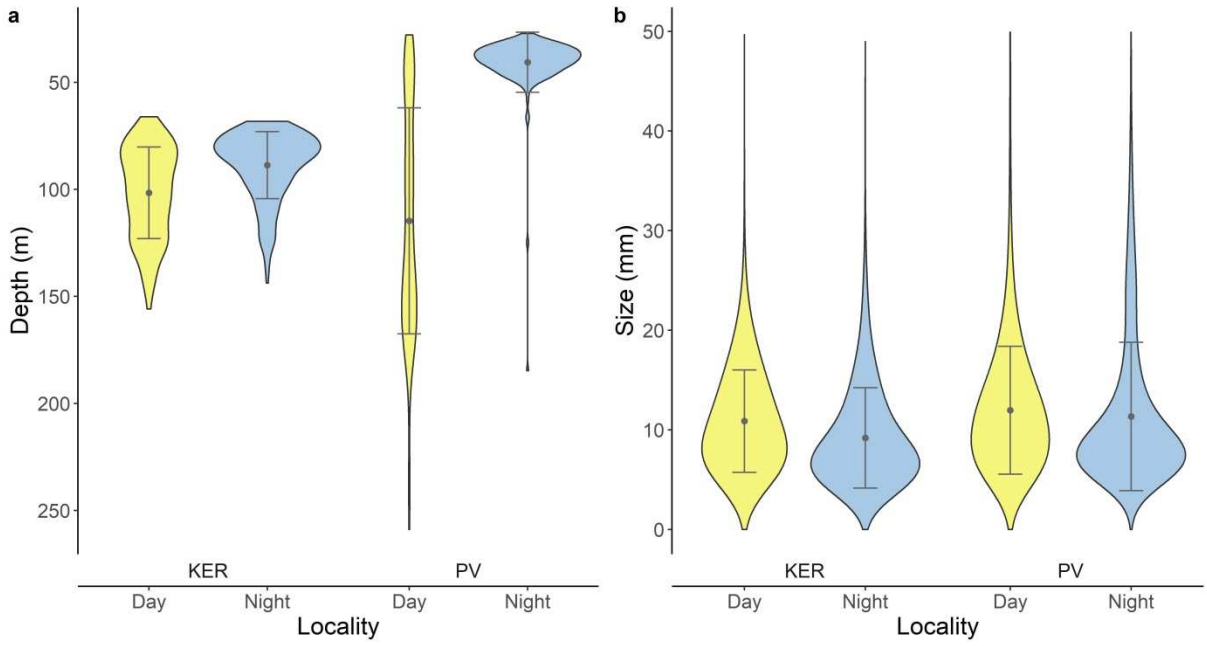

Figure 10: (a) Mean day (yellow) and night (blue) DVM depth for the 2 locations. The DVM depth is the depth with the maximum density over a profile. (b) Mean particle size distribution over thedepth range (70:260). Grey points indicate the mean and the error bars represent +/-1 standard deviation.

Supplementary information

Calculation of the sonar tag metrics:

Intensity threshold definition:

The noise intensity threshold is set on the last meter of the sonar detection range (5 to 6m), assuming that the entire signal in this range is ambient noise, and designated as the Background Noise Level (BNL).

The amplitude fluctuations in the signal obtained from a shadow area (i.e. area behind a target) or from out-of-range detections are essentially electronic noise. The signal amplitude X is thus noised with a Gaussian distribution function.

$$G(X) = \frac{1}{\sqrt{2\pi\sigma}} exp \frac{-(X-\mu)^2}{2\sigma^2}$$

where μ is the mean of the amplitude and σ the standard deviation.

The acoustic signal recorded by the sonar tag is the result of a combination of elementary signals, which can be for example caused by a strong scattering phenomenon. For the sonar tag, two signal channels of different amplitudes are considered, the sum of these constituting the acoustic signal. The signal amplitude R resulting in the sum of the channels is described as a Rayleigh law.

$$R = \sqrt{X^2 + Y^2}$$

with $X \sim \mathcal{N}(0, \sigma^2)$ and $Y \sim \mathcal{N}(0, \sigma^2)$

Then $R \sim Rayleigh(\sigma)$

A random sampling of the BNL is operated over the entire record, with 1000 pixels values (acoustic power) sampled over a continuous sonar record sequence of at least 10 minutes. The sizes of the samples for KER and PV records are 10.10^7 and 13.10^7 respectively. The cumulative distribution function of the Rayleigh law is fitted upon the BNL samples (Figure 2). The threshold is set as the acoustic power value (μPa) corresponding to the 99.9^{th} percentile of the Rayleigh distribution (for KER and PV), allowing the discrimination between the actual target detection and the white noise in the studied range 1-1.5m of the sonar beam.

1090

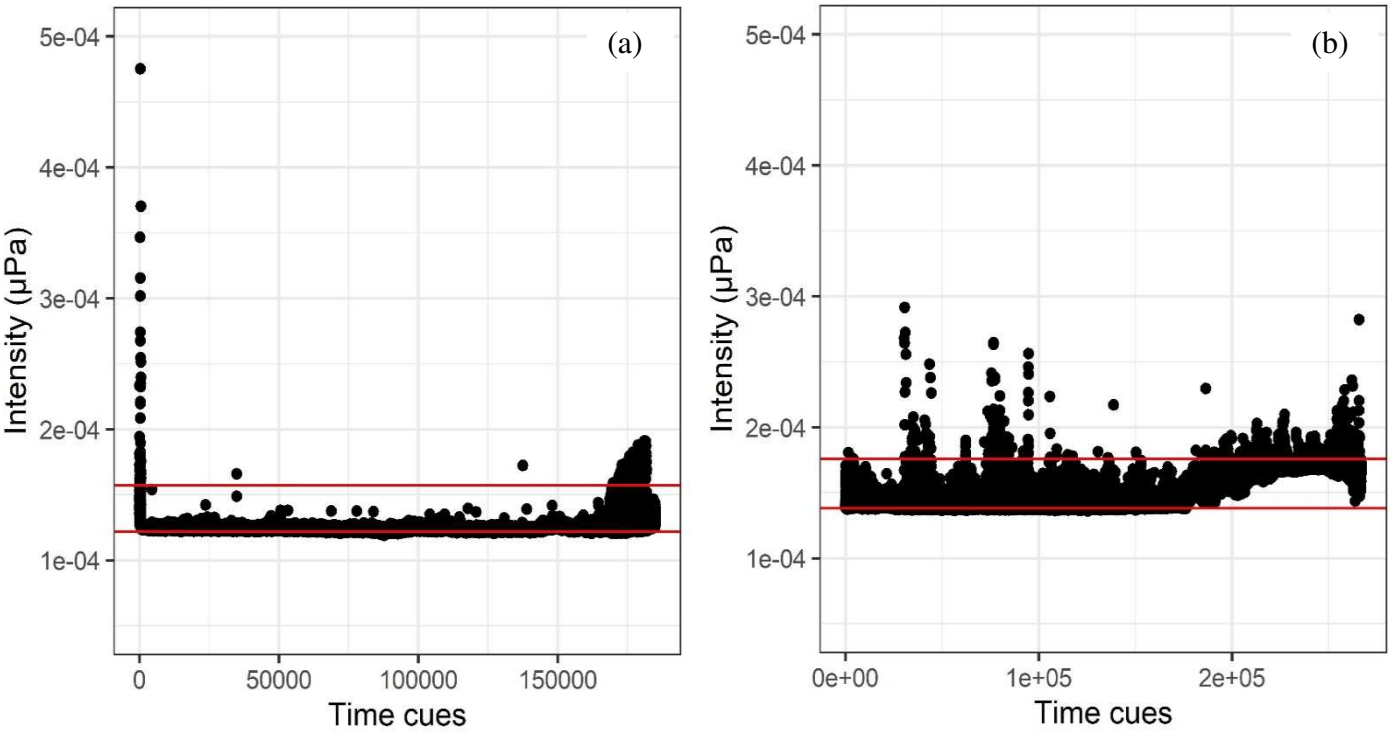

1091

1092 Figure 1: Time series of the Background Noise Level (BNL) for (a) KER and (b) PV. The
1093 interval between the red lines contains 99,9% of the sampled echoes, which are used to fit the
1094 Rayleigh distribution.

1095

1096 The far range of the sonar beam is unlikely to insonify target. But it could sometimes happen
1097 that the far range contains a few targets, particularly in regions with high target densities. The
1098 evolution of the background sampled values is represented in Figure 1. To prevent the
1099 influence of peaks or trends in the signal, the 1 % of extreme values are removed to prevent
1100 the influence of peaks or trends in the BNL threshold calculation.

1101

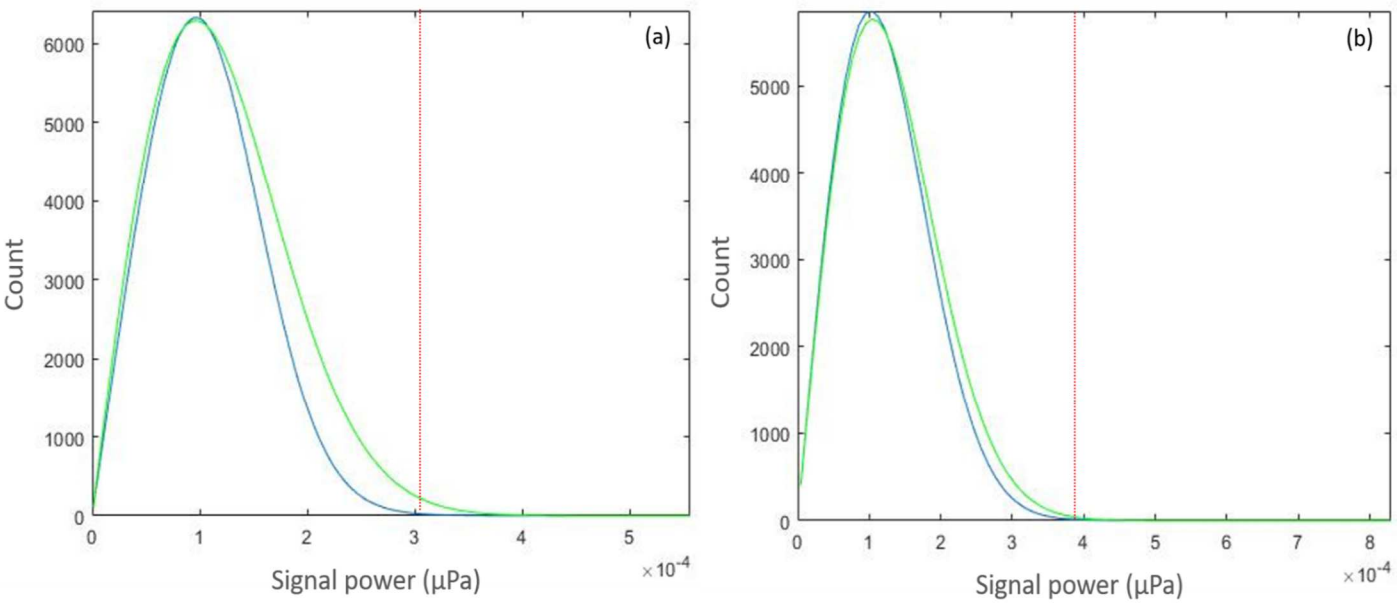

Figure 2: Rayleigh fit of the data for KER (a) and PV (b) Background Noise Level (BNL) sampled in the last meter of the signal range. The green line represents the density probability for a theoretical Rayleigh distribution, and the blue lines the fitted distribution of the samples. The vertical dotted red lines represent the defined threshold, set as the quantile 99,9% of the Rayleigh distribution.

Echo Intensity distribution

The echo intensity presented in figure 3 is expressed as the echo-integration of each ping of the records. The echo-integration is performed by summing the echo power of each 4mm bin insonified in the range 1m – 1.5m.

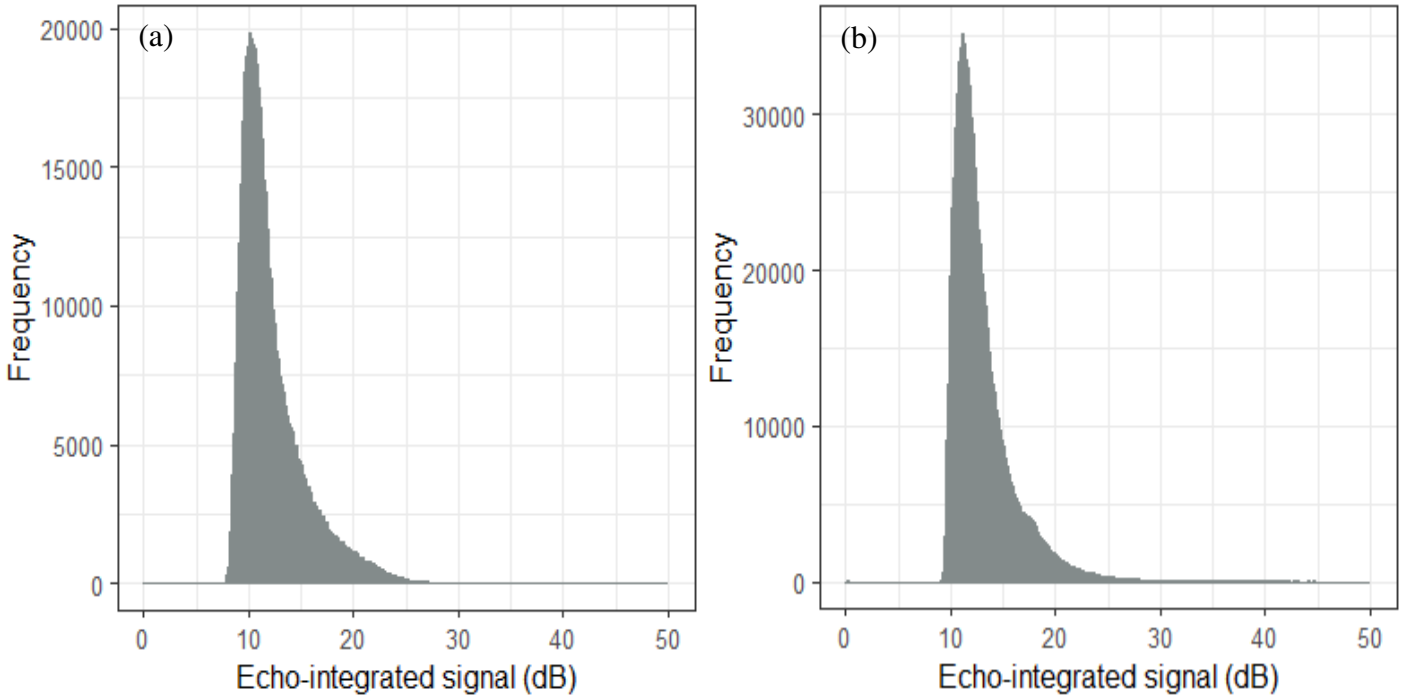

Figure 3: Distribution of the echo integrated intensities for (a) KER and (b) PV sonar records.

Minimum size detected

The ability of the sonar to detect small targets at the limit of the sensor resolution depends primarily on its position in the beam and the acoustic backscattering properties of its body. However, size is the most common measure to discriminate organisms, but fluid-like organisms - even of large size - cannot be observed, thus we propose a limit of detectability for small targets with high Signal-to Noise-Ratio.

The sonar was deployed simultaneously with an optical sensor (Underwater Vision Profiler UVP5) in the Mediterranean Sea for an efficient measurement of the size of the targets. The

density profiles show a maximum correlation for a target size class greater than 1mm, with the same density peaks at 47.5m and 147.5m deep for both instruments (Figure 4). Targets identified as detritus from the UVP images contribute to a large part of the signal and suggest that they are detectable by sonar for sizes larger than 1mm.

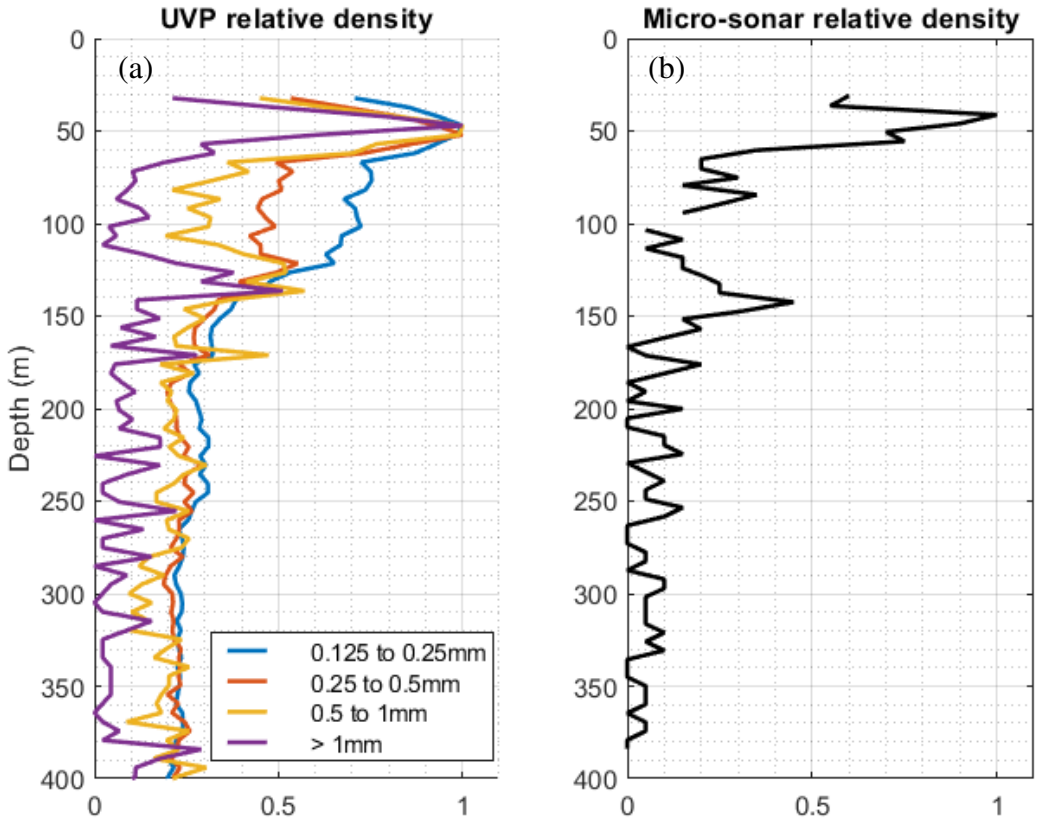

Figure 4: Relative density of detected targets simultaneously by (a) an Underwater Vertical Profiler (UVP) and (b) the sonar tag attached to the UVP along a vertical profile. Colored curves represent the relative density of detected targets belonging to a specific size class.

Dives clustering:

A dive is considered when the animal is continuously deeper than 15m. After the B-spline reconstruction and the FPCA performed on the B-spline coefficients, the observations (profiles) were projected in the space of the first two PCs (Figure 5). The five first components explained 98% and 91.5% of the total inertia for KER and PV respectively. By adding or subtracting the eigenfunctions to the mean profile, one can assess the effect of the principal components on the curve shape (Figure 6). For each component, if an observation is in the positive part of the PC axis, the shape of this observation should be close

to the one described by the '+' curve. Inversely, negatives observations on the PC axis would have a curve close to the one described by the '-'.

Before the *k*-means classification, the optimal number of *k* clusters was determined using the Ward distance, minimizing the total within-cluster variance, on the observations. A visual assessment of the cluster tree allowed retaining 3 clusters for both KER (Figure 7) and PV (Figure 8).

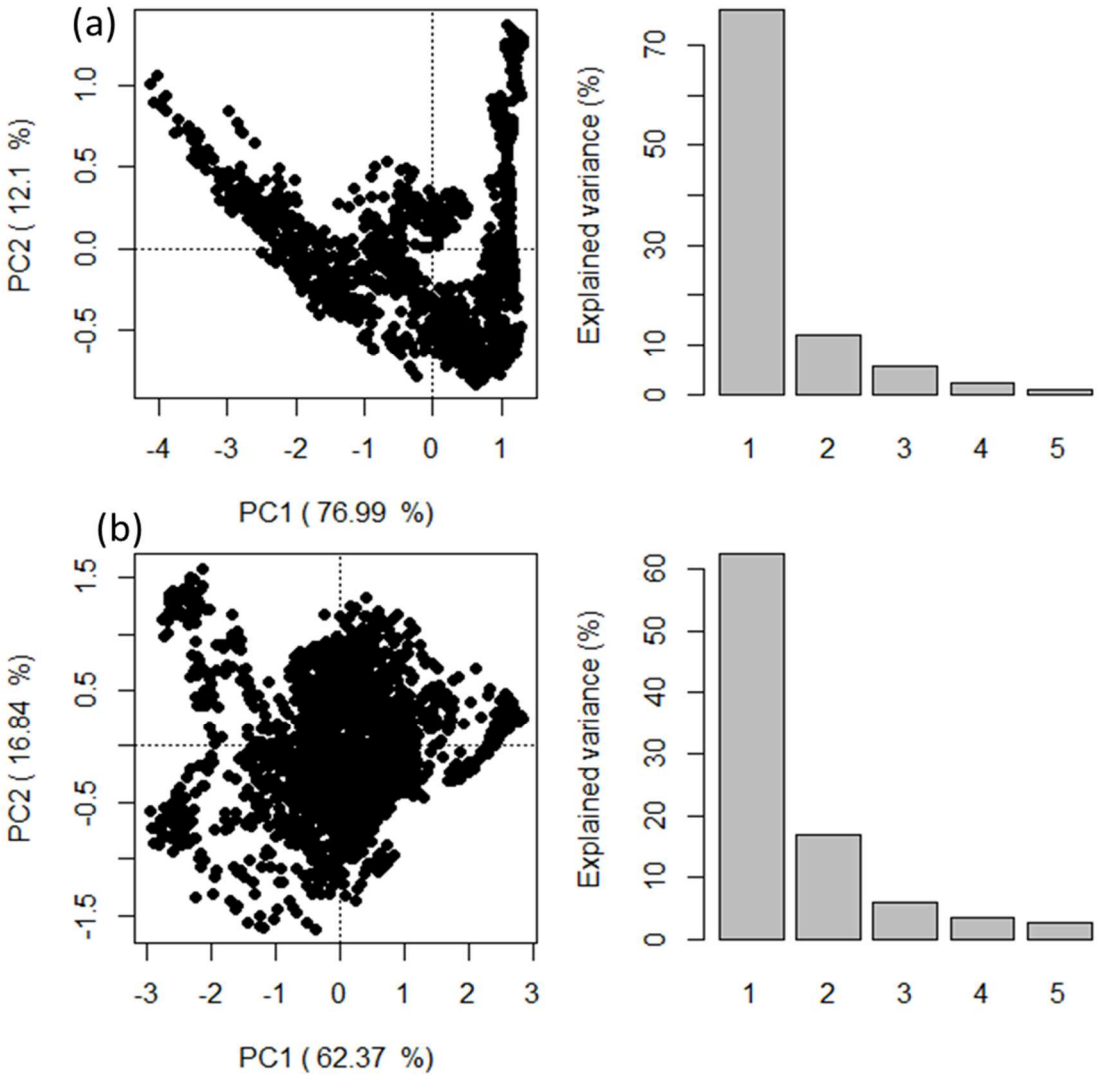

Figure 5: Left: Temperature-Salinity profiles represented over the space of the first two modes of the FPCA for KER (a) and PV (b). Right: Percentage of the variance explained by the first 5 eigenfunctions of the FPCA.

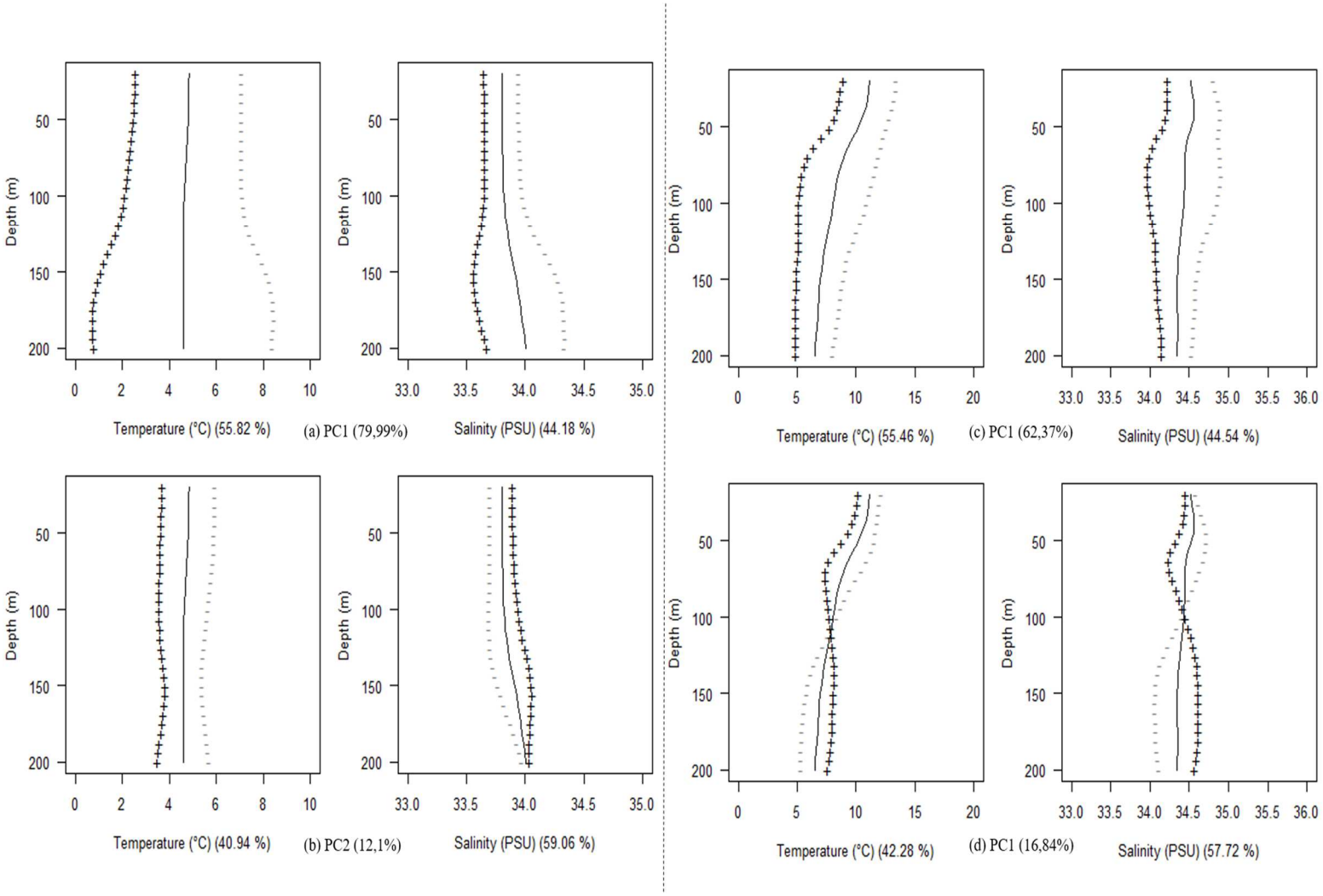

Figure 6: Representation of the effects of the first two eigenfunctions on temperature and salinity mean profiles, for KER (a,b) and PV (c,d). The curves show the mean profile (solid) and the effect of adding (+) and subtracting (-) the first (a,c) and the second (b,d) eigenfunctions. The percentages indicated in the x-axis label are the variance contained by each variable (T and S) for the corresponding component.

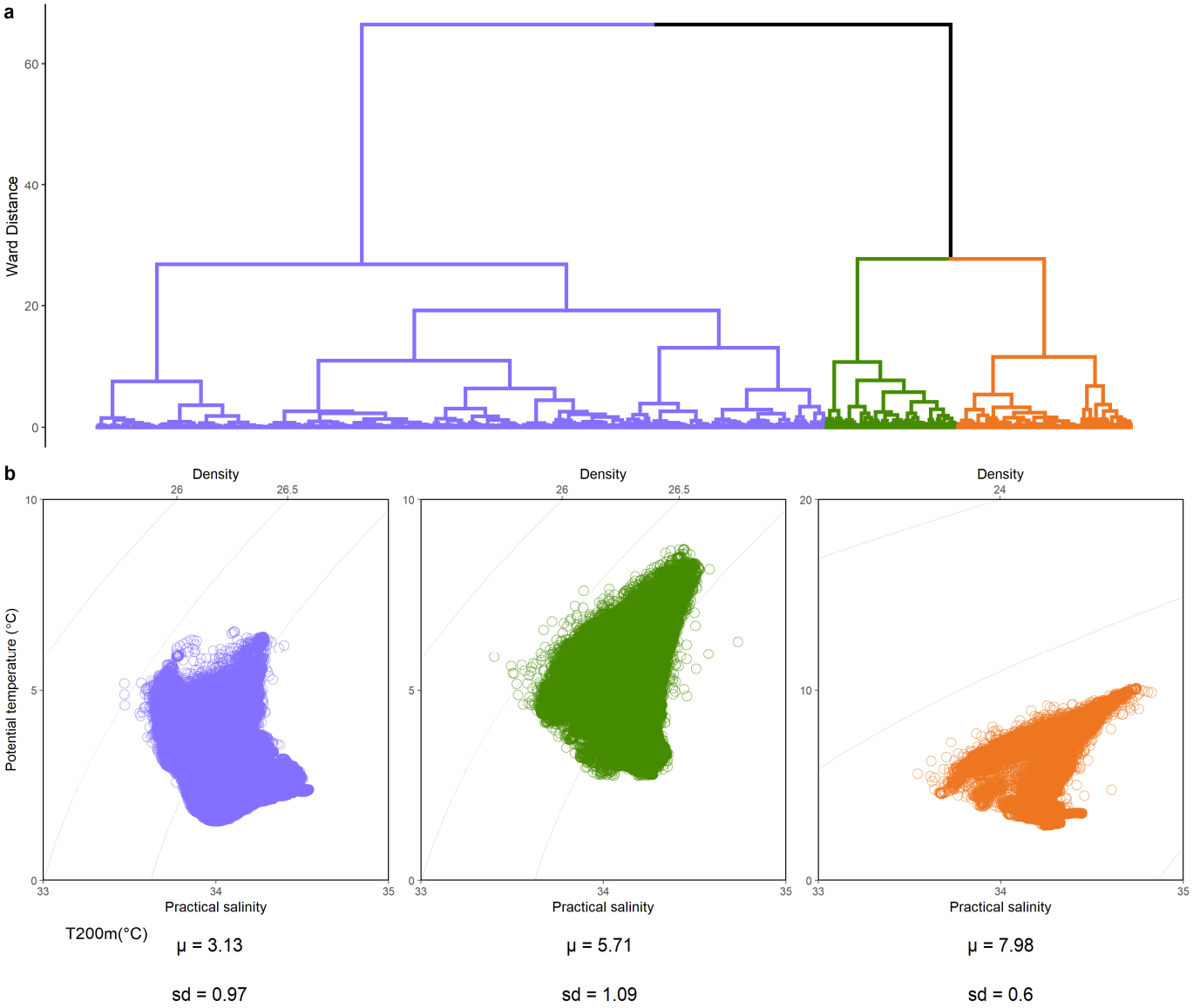

Figure 7: Cluster resulting of the *k*-means classification for KER. The hierarchical clustering tree, defined by the Ward distance, suggesting an optimal clustering in 3 groups: cluster 1 (purple), cluster 2 (orange), and cluster 3 (green). (b) T-S diagrams of all profiles contained in each cluster, associated with the mean 200m-deep and the standard deviation of the temperature.

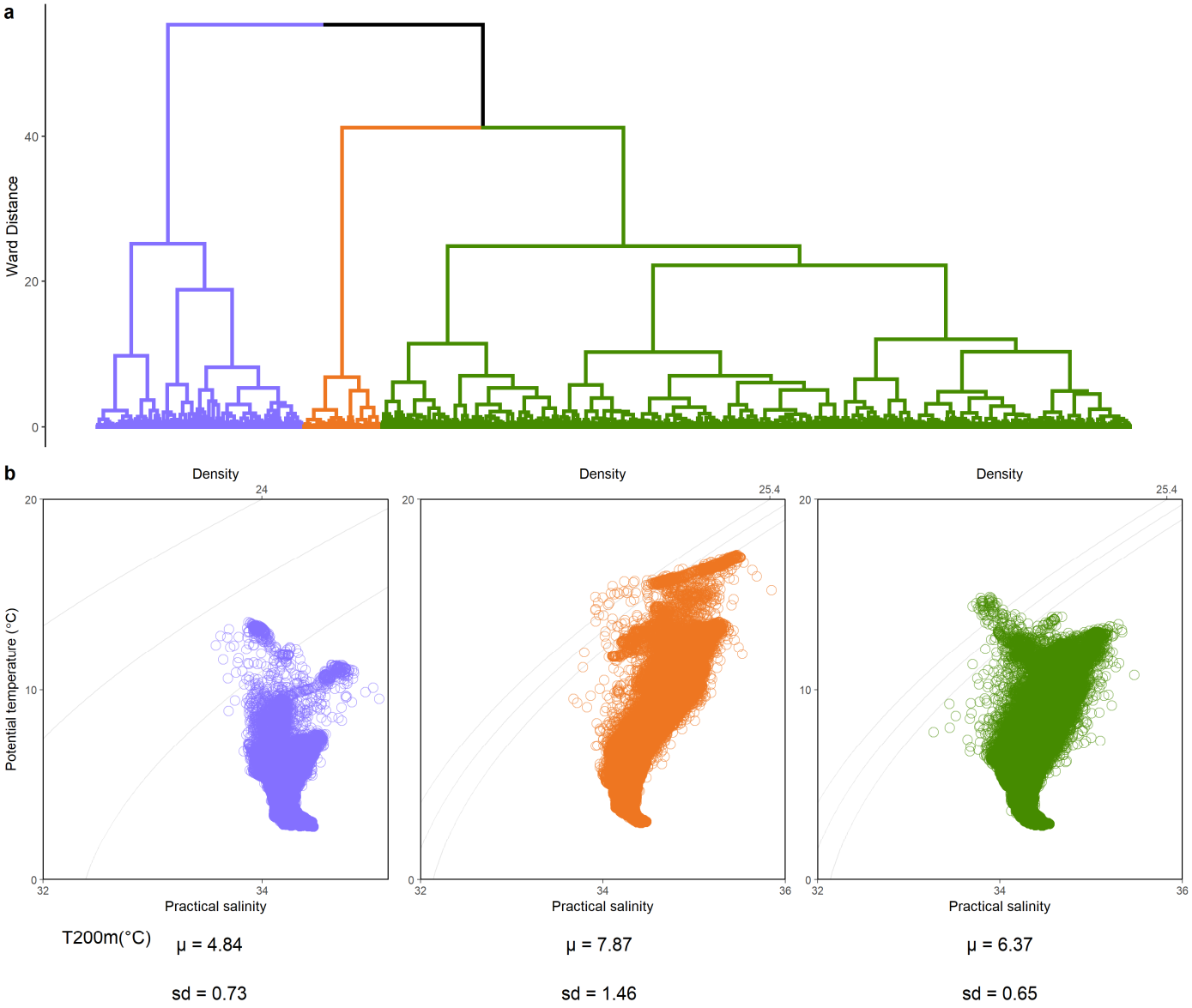

1167
1168 Figure 8: Cluster resulting of the *k*-means classification for PV. The hierarchical clustering tree,
1169 defined by the Ward distance, suggesting an optimal clustering in 3 groups: cluster 1 (purple),
1170 cluster 2 (orange), and cluster 3 (green). (b) T-S diagrams of all profiles contained in each
1171 cluster, associated with the mean 200m-deep and the standard deviation of the temperature.
1172
1173
1174 Table 1: Mean temperature and salinity with standard deviations recorded at 200m deep for
1175 each water masses in both locations.

Location	KERGUELEN			PENINSULA VALDES		
Cluster (water mass)	1	2	3	1	2	3
Temperature	3.1°C	5.7°C	8°C	4.8°C	6.4°C	7.9°C

(T200m)	(±0.1)	(±1.1)	(±0.6)	(±0.7)	(±0.6)	(±1.4)
Salinity (S200m)	33.9‰ (±0.08)	34.1‰ (±0.14)	34.4‰ (±0.1)	34.2‰ (±0.07)	34.4‰ (±0.2)	34.6‰ (±0.3)

1176
1177
1178